

# Evaluation of Dip Angles of Active Faults Beneath the Osaka Plain Inferred from a 2D Numerical Analysis of visco-elasto-plastic Models

**Hayami Nishiwaki**

Osaka City University: Osaka Shiritsu Daigaku

**Takamoto Okudaira** (✉ [oku@sci.osaka-cu.ac.jp](mailto:oku@sci.osaka-cu.ac.jp))

Osaka City University: Osaka Shiritsu Daigaku <https://orcid.org/0000-0002-6695-6246>

**Kazuhiko Ishii**

Osaka Prefecture University

**Muneki Mitamura**

Osaka City University: Osaka Shiritsu Daigaku

---

## Full paper

**Keywords:** dip angle, fault geometry, visco-elasto-plastic simulation, Uemachi fault zone, Ikoma fault zone, Osaka Group, Osaka Plain, 2018 northern Osaka earthquake, active fault, seismogenic source fault

**Posted Date:** September 24th, 2020

**DOI:** <https://doi.org/10.21203/rs.3.rs-79376/v1>

**License:**  This work is licensed under a Creative Commons Attribution 4.0 International License.

[Read Full License](#)

---

1 Evaluation of dip angles of active faults beneath the Osaka Plain inferred from a

2 2D numerical analysis of visco-elasto-plastic models

3

4 Hayami Nishiwaki, Department of Geosciences, Osaka City University, Osaka 558–

5 8585, Japan, m19sco19@jr.osaka-cu.ac.jp

6 Takamoto Okudaira, Department of Geosciences, Osaka City University, Osaka 558–

7 8585, Japan, oku@sci.osaka-cu.ac.jp, ORCID iD: 0000-0002-6695-6246

8 Kazuhiko Ishii, Department of Physical Sciences, Osaka Prefecture University, Sakai

9 599–8531, Japan, ishii@p.s.osakafu-u.ac.jp, ORCID iD: 0000-0002-4172-1248

10 Muneki Mitamura, Department of Geosciences, Osaka City University, Osaka 558–

11 8585, Japan, mitamura@sci.osaka-cu.ac.jp, ORCID iD: 0000-0002-6875-439X

12

13 Correspondence: Nishiwaki H, Okudaira T

14

15 **Abstract**

16 The geometries (i.e., dip angles) of active faults from the surface to the seismogenic  
17 zone are among the most important factors used to evaluate earthquake ground motion,  
18 which is crucial to seismic hazard assessments in urban areas. In Osaka, a metropolitan  
19 city in Japan, there are several active faults (e.g., the Uemachi and Ikoma faults), which  
20 are inferred from the topography, the attitude of active faults in surface trenches, the  
21 seismic reflection profile at shallow depths (less than 2 km), and the three-dimensional  
22 distribution of the Quaternary sedimentary layers. The Uemachi and Ikoma faults are  
23 N–S-striking fault systems with total lengths of 42 km and 38 km, respectively, with the  
24 former being located ~12 km west of the latter; however, the geometries of each of the  
25 active faults within the seismogenic zone is not clear. In this study, to examine the  
26 geometries of the Uemachi and Ikoma faults from the surface to the seismogenic zone,  
27 we analyze the development of the geological structures of sedimentary layers based on  
28 numerical simulations of a two-dimensional visco-elasto-plastic body under a horizontal  
29 compressive stress field, including preexisting linear high-strained weak zones (i.e.,  
30 faults) and surface sedimentation processes, and evaluate the relationship between the

31 observed geological structures of the Quaternary sediments (i.e., the Osaka Group) in  
32 the Osaka Plain and the model results. Based on a comparison between the simulation  
33 results and the geological observations/interpretation, we propose geometries of the  
34 Uemachi and Ikoma faults from the surface to the seismogenic zone. When the friction  
35 coefficient of the faults is  $\sim 0.5$ , the dip angles of the Uemachi and Ikoma faults near the  
36 surface are  $\sim 30^\circ\text{--}40^\circ$  and the Uemachi fault has a downward convex curve at the  
37 bottom of the seismogenic zone but does not converge to the Ikoma fault. Based on the  
38 analysis in this study, the dip angle of the Uemachi fault zone is estimated to be  
39 approximately  $30^\circ\text{--}40^\circ$ , and the downward extension of the Uemachi fault zone nearly  
40 coincides with the epicenter of the 2018 northern Osaka earthquake.

41

42 **Keywords:** dip angle, fault geometry, visco-elasto-plastic simulation, Uemachi fault  
43 zone, Ikoma fault zone, Osaka Group, Osaka Plain, 2018 northern Osaka earthquake,  
44 active fault, seismogenic source fault

45

46 **Introduction**

47 The 2018 northern Osaka earthquake that occurred on June 18, 2018, was located at the  
48 junction of the Arima-Takatsuki fault zone and the Ikoma fault zone. The focal  
49 mechanism solution for this earthquake showed a N–S-striking reverse fault type (Kato  
50 and Ueda 2019). If the dip angle of the Uemachi fault zone, which is a reverse fault with  
51 a N–S strike and E dip, is approximately  $40^\circ$ , the downward extension of the Uemachi  
52 fault zone would nearly coincide with the epicenter of the earthquake (Fig. 1). However,  
53 the relationship between this earthquake and the Uemachi fault zone is still unknown  
54 because the attitude (i.e., the strike and dip angle) of the Uemachi fault zone at the depth  
55 of the seismogenic zone is not well understood. Similar to the Uemachi fault zone, the  
56 attitude of active faults, including the Ikoma fault zone, in the Osaka Plain within the  
57 seismogenic zone (at a depth of  $\sim 10\text{--}15$  km) is not clear. The topography, the attitudes  
58 of active faults in surface trenches, seismic reflection profiles at shallow depths (less  
59 than 2 km), and the three-dimensional distribution of the Quaternary strata based on  
60 bored geological columns have been used by the Headquarters for Earthquake Research  
61 Promotion of MEXT and the Central Disaster Prevention Council to evaluate the  
62 activities of each active fault. The deep underground attitudes of active faults have been

63 estimated assuming that the attitude near the surface hardly changes with depth (e.g.,  
64 Headquarters for Earthquake Research Promotion of MEXT 2001, 2004; Director  
65 General for Disaster Management 2006; Fig. 1). To mitigate earthquake damage, it is  
66 essential to predict ground motion caused by earthquakes that occur on active faults,  
67 and the attitude of the source fault in the seismogenic zone is the most important factor  
68 used to predict the ground motion.

69 To estimate the dip angles of the active faults at depth in the Osaka Plain, numerical  
70 analyses were performed to determine how the deformation of the strata and the ground  
71 surface changes as a result of different fault dip angles; the simulation results can be  
72 compared to the distribution of the strata in the Osaka Group and the inclination angle  
73 of the axial plane of the subsurface flexure of the Uemachi fault (Ishiyama 2003;  
74 Iwasaki 2016; Fig. 1). However, these different dip angles were obtained by forcibly  
75 deforming the pre-deposited strata via displacement at the fault; factors, such as the  
76 fault behavior under the assumed stress field, the rheological properties of the rocks and  
77 sediments, and sedimentation and erosion, have not been considered.

78 In this study, to examine the geometries of the Uemachi and Ikoma faults at the depth

79 of the seismogenic zone, we analyze the development of geological structures in the  
80 sedimentary layers based on numerical simulations of a two-dimensional  
81 visco-elasto-plastic body under a horizontal compressive stress field, including  
82 preexisting linear high-strained weak zones (i.e., faults) and surface sedimentation  
83 processes, and evaluate the relationship between the observed geological structures of  
84 the Quaternary sediments (i.e., the Osaka Group) in the Osaka Plain and the model  
85 results.

86

#### 87 **Constraints on the numerical simulation: Quaternary geology in the Osaka Plain**

88 The Osaka sedimentary basin is an oval topographical depression surrounded by  
89 mountains, and the Osaka Bay and the Osaka Plain are located in its western and eastern  
90 regions, respectively. The boundary between the Osaka Plain and the surrounding  
91 mountains is demarcated to the north by the ENE–WSW-trending Arima-Takatsuki fault  
92 zone and to the east by the N–S-trending Ikoma fault zone. The N–S-trending Uemachi  
93 fault zone is located in the central part of the Osaka Plain (Fig. 2a). Quaternary crustal  
94 deformation in and around the Osaka sedimentary basin is referred to as the Rokko

95 movements (Ikebe and Huzita 1966; Huzita 1968, 1990) and result from the subduction  
96 of the Pacific Plate at the Japan Trench and that of the Philippine Sea Plate at the  
97 Nankai Trough (Huzita 1968; Itoh et al. 2000). Based on a comparison between the  
98 present stress conditions, the direction of the horizontal maximum stress ( $\sigma_{H_{max}}$ ) is  
99 currently nearly E–W (Tsukahara and Kobayashi 1991; Terakawa and Matsu'ura 2010),  
100 and the conditions determined by inverting the fault-slip data from active faults that  
101 have exhibited cumulative displacement for the past  $\sim 10^5$  years, it has been suggested  
102 that the stress field in central Japan has been uniform and stable for the past  $\sim 10^5$  years  
103 (Tsutsumi et al. 2012). Wesnousky et al. (1982) estimated the geological horizontal  
104 shortening strain rate of central Japan, including in the Kinki region, to be  $16\text{--}26 \times$   
105  $10^{-9}/\text{yr}$ , based on earthquake records with a magnitude of 6.9 or greater and the  
106 displacement rates of active faults for the last  $\sim 400$  years. We first summarize the  
107 Quaternary geology in the Osaka Plain, especially that of the Osaka Group, Uemachi  
108 fault zone, and Ikoma fault zone, because the geometry in these regions constrains the  
109 model parameters and results.

110

111 **Osaka Group**

112 The Osaka sedimentary basin is filled by the strata of the Plio–Middle Pleistocene  
113 Osaka Group, Middle–Upper Pleistocene terrace deposits and their corresponding  
114 sediments, and Upper Pleistocene–Holocene alluvium. The strata are 1,000–2,000-m  
115 thick at the deposition center and 200–400-m thick at the margins (Itihara 1993).  
116 Yoshikawa and Mitamura (1999) reported that the Quaternary system in the Osaka Plain  
117 consists of unconsolidated clay, silt, sand, and gravel layers with a thickness of more  
118 than 1,500 m and dozens of volcanic ash layers; this system has been divided into the  
119 Miyakojima Formation in the lower part, the Tanaka Formation in the upper part, and  
120 the Namba Formation in the uppermost part (Fig. 2b). The Miyakojima Formation  
121 consists of freshwater layers primarily composed of gravel, sand, and silt layers,  
122 whereas the Tanaka and Namba formations consist of freshwater sand and gravel layers  
123 and 21 marine clay layers (Ma-1, Ma0, Ma0.5, Ma1, Ma1.3, Ma1.5, Ma1.7, Ma2,...,  
124 Ma11 (1), Ma11 (2), Ma12, and Ma13).

125 Since the 1995 Hyogoken-Nambu earthquake, multiple drilling and seismic  
126 reflection surveys have been conducted in the Osaka Plain, revealing details concerning

127 its subsurface structure. Ikebe et al. (1970) analyzed nine deep drilling cores (OD-1–  
128 OD-9) and found that the Osaka Plain can be divided into two areas (i.e., west and east  
129 Osaka) by the N–S-trending Uemachi fault zone running through the central part of the  
130 plain. The basement depth in west Osaka is more than 1,000 m (because the OD-1 core  
131 did not reach basement rock at a depth of 907 m), whereas the basement depth in the  
132 Uemachi Upland and its northern extension is as shallow as 656 m (OD-2; Fig. 2b). The  
133 basement depth in the central part of the Osaka Plain was examined based on the  
134 basement structures inferred from gravity anomalies (Nakagawa et al. 1996a; Kansai  
135 Geo-informatics Council 1998) and reflection seismic surveys (Ikebe et al. 1970). Using  
136 this information, Uchiyama et al. (2001) and the Osaka Prefecture (2004) found that the  
137 depth of the basement surface in west Osaka is nearly 1,500 m and does not  
138 significantly change to the west; meanwhile, in east Osaka, the depth is approximately  
139 800 m near the Uemachi Upland and more than 1,500 m near the Onchi River and the  
140 surface of the basement slopes to the east (Fig. 3). In addition, the strata thickness does  
141 not change in west Osaka, whereas the strata thickness in east Osaka tends to increase  
142 eastward (Uchiyama et al. 2001). In detail, in east Osaka, the thickness of the

143 Miyakojima Formation is approximately 550 m at the Uemachi Upland and more than  
144 700 m near the Onchi River and the thickness of the lower Tanaka Formation (Ma-1–  
145 Ma6) is approximately 250 m at the Uemachi Upland and 850 m near the Onchi River.

146 According to Uchiyama et al. (2001), the sedimentation rate from ~1.2 million to  
147 ~0.05 million years ago (Ma) in west Osaka, obtained from the OD-1 core, gradually  
148 decreased from 0.7 m/kyr to 0.2 m/kyr and the rate of the decrease in the sedimentation  
149 rate was higher after ~0.4 Ma. In east Osaka, in the western region near the Uemachi  
150 Upland (OD-2, OD-9, and YU), the sedimentation rate from ~1.2 Ma to ~0.6 Ma,  
151 corresponding to the lower Tanaka Formation, decreases from 0.5 m/kyr to 0.3 m/kyr,  
152 whereas the sedimentation rate decreases from 0.8 m/kyr to 0.5 m/kyr in the eastern  
153 region (OD-3). The Tanaka Formation around the Uemachi Upland is preserved in  
154 conformity only from the Ma3 layer to the Ma7 layer and is partially covered in an  
155 unconformity by the Ma12 layer. Suzuki (2016) estimated the sedimentation rate of the  
156 Miyakojima Formation to be 0.48 m/kyr using the deep drilling core data of Yoshikawa  
157 et al. (2000).

158

159 **Uemachi fault zone**

160 The Uemachi fault zone is a nearly N–S-striking fault system with a total length of 42  
161 km, including the Butsunenji-yama fault, Uemachi fault, Nagai fault, Sakamoto fault,  
162 Kumedaïke fault, Sakuragawa flexure, and Suminoe flexure. It is a reverse fault in  
163 which the eastern side of the fault zone has moved upward relative to the western side  
164 (Nakada et al. 1996a, 1996b, 1996c, 1996d; Okada and Togo 2000). It has been  
165 confirmed that the Uemachi fault zone has cut up to the Ma12 layer (Mitamura et al.  
166 1994) and that the Holocene sediments near the surface are bent (Headquarters for  
167 Earthquake Research Promotion of MEXT 2004). The dip angle of the fault has been  
168 estimated to be 65°–70° (Headquarters for Earthquake Research Promotion of MEXT  
169 2004), as inferred from topographical and geological features (Huzita and Kasama  
170 1982) and the results of seismic reflection surveys (e.g., Sugiyama and Sangawa 1996;  
171 Sugiyama, 1997; Sugiyama et al. 2001, 2003). Based on the difference in the thickness  
172 of the Quaternary strata between the eastern and western sides of the Uemachi fault, the  
173 displacement rate of the Uemachi fault zone from 1.2 Ma to 0.6 Ma has been estimated  
174 to be ~0.3 m/kyr (Uchiyama et al. 2001) while that from 0.6 Ma to 0.15 Ma has been

175 estimated to be ~0.4 m/kyr (Headquarters for Earthquake Research Promotion of  
176 MEXT 2001).

177 Ishiyama (2003), based on the seismic reflection survey of Yoshikawa et al. (1987),  
178 interpreted the bending structure of the reflection section as a fault-propagation fold.  
179 Given that the Uemachi fault has a dip angle of ~40° and that there is 1 km of slip along  
180 the fault, he demonstrated, using the trishear fault-propagation fold model of  
181 Allmendinger (1998), that the sedimentary structure of the Ma-1 layer at the lowermost  
182 part of the Tanaka Formation can be reproduced. Furthermore, because the Osaka Group  
183 is thinner at the Uemachi Upland and thicker eastward, Ishiyama (2003) suggested that  
184 the Uemachi fault zone may be a thin-skinned thrust converging to a low-angle  
185 detachment in the upper crust (less than 5 km; Fig. 1). Sato et al. (2009) interpreted the  
186 seismic reflection results to indicate that the Uemachi and Ikoma fault zones inclined to  
187 the east and that their low-angle detachment faults converge at a depth of approximately  
188 10 km, which is much deeper than the depth suggested by Ishiyama (2003). Iwasaki  
189 (2016) evaluated the dip angle of the Uemachi fault using PLAXIS®, a finite element  
190 method ground analysis software. Given a displacement of several meters along the

191 fault with a dip angle of  $\sim 30^\circ$  and with the fault tip located 1,000 m below the surface,  
192 the inclination angle of the axial plane of the Sakuragawa flexure ( $65^\circ\text{--}70^\circ$ ) can be  
193 reproduced.

194

### 195 **Ikoma fault zone**

196 The Ikoma fault zone is a nearly N–S-striking fault system with a total length of 38 km.  
197 It is composed of the Ikoma fault, Katano fault, Hirakata fault, Taguchi fault, and Konda  
198 fault (Nakada et al. 1996a, 1996b; Okada et al. 1996; Shimokawa et al. 1997; Sugiyama  
199 et al. 1999; Okada and Togo 2000). At the surface, the Ikoma fault is located  $\sim 12$  km  
200 east of the Uemachi fault (Fig. 2a) The Ikoma fault is an east-side-up reverse fault  
201 located near the boundary between the Osaka Plain and the Ikoma Mountains, which  
202 consist of rocks of the Ryoke belt (Horike et al. 1995; Nakata et al. 1996a, 1996b;  
203 Shimokawa et al. 1997). Active faults are inferred from the fact that the low fault cliff  
204 that cuts the lower terrace runs alongside the Ikoma fault approximately 0.5–1 km to its  
205 west, with the location of the fault estimated along the slope transformation line that  
206 transitions from the mountain slope to the fan; the inferred active faults are thought to

207 be more important in the Holocene than the fault along the mountain slope (Okada and  
208 Yagi 2019; Okada and Togo 2000). Using seismic reflection surveys at the Ikoma fault,  
209 Shimokawa et al. (1997) found that the Ikoma fault is inclined to the east at a moderate  
210 angle (approximately  $30^{\circ}$ – $40^{\circ}$ ) below a depth of 400 m. Furthermore, they estimated the  
211 mean vertical displacement rate of the Ikoma fault system to be 0.5–1 m/kyr, as inferred  
212 from a trench survey. Ishiyama (2003) suggested that the high uplift rate of the Ikoma  
213 fault zone indicates thick-skinned trajectories. He also pointed out that the downward  
214 projection of the Uemachi fault zone soles into the Ikoma fault in the shallower portion  
215 of the crust, suggesting that the northern Uemachi fault zone and the Ikoma fault zone  
216 comprise a larger system of a west-verging active fold and thrust belt that  
217 accommodates E–W contraction within the upper crust and that the Uemachi fault zone  
218 is a leading edge of the thrust belt.

219

## 220 **Numerical simulations**

### 221 **Method**

222 Numerical simulations of a two-dimensional visco-elasto-plastic body were performed

223 using the I2ELVIS code of Gerya and Yuen (2003, 2007) and Gerya (2010) for

224 MATLAB<sup>®</sup>, with the deviatoric strain rate,  $\dot{\epsilon}_{ij}$ , including three components:

225

$$226 \quad \dot{\epsilon}_{ij} = \dot{\epsilon}_{ij(\text{viscous})} + \dot{\epsilon}_{ij(\text{elastic})} + \dot{\epsilon}_{ij(\text{plastic})}, \quad (1)$$

227

228 where

229

$$230 \quad \dot{\epsilon}_{ij(\text{viscous})} = \frac{1}{2\eta} \sigma_{ij}, \quad (1a)$$

231

$$232 \quad \dot{\epsilon}_{ij(\text{elastic})} = \frac{1}{2G} \frac{D\sigma_{ij}}{Dt}, \quad (1b)$$

233

$$234 \quad \dot{\epsilon}_{ij(\text{plastic})} = 0 \text{ for } \sigma_{II} < \sigma_{\text{yield}},$$

$$235 \quad \dot{\epsilon}_{ij(\text{plastic})} = \chi \frac{\sigma_{ij}}{2\sigma_{II}} \text{ for } \sigma_{II} = \sigma_{\text{yield}}, \quad (1c)$$

236

237 where  $\eta$  is the effective viscosity,  $G$  is the shear modulus,  $D\sigma_{ij}/Dt$  is the objective

238 co-rotational time derivative of the deviatoric stress component  $\sigma_{ij}$ ,  $\sigma_{\text{yield}}$  is the plastic

239 yield strength for a given rock,  $\sigma_{II} = (1/2\sigma_{ij}\sigma_{ij})^{1/2}$  is the second deviatoric stress invariant,

240 and  $\chi$  is the plastic multiplier.

241 To yield an effective rheology, the Mohr–Coulomb law was simplified using the

242 yield stress,  $\sigma_{\text{yield}}$ , criterion and implemented using a “Mohr–Coulomb viscosity”,  $\eta_{\text{MC}}$ ,

243 as follows:

244

$$245 \quad \eta_{\text{MC}} = \sigma_{\text{yield}} / (2\dot{\epsilon}_{II}), \quad (2)$$

246

247 where  $\dot{\epsilon}_{II} = (1/2\dot{\epsilon}_{ij}\dot{\epsilon}_{ij})^{1/2}$  is the second invariant of the strain rate tensor. The yield

248 stress or plastic strength,  $\sigma_{\text{yield}}$ , of a rock generally depends on the mean stress on the

249 solids,  $P$ , such that

250

$$251 \quad \sigma_{\text{yield}} = C + \sin(\varphi)P, \quad (3)$$

252

253 where  $C$  is the cohesion (the residual strength at pressure  $P = 0$ ) and  $\varphi$  is the effective

254 internal friction angle. The effective viscosity,  $\eta$ , is then defined using the following

255 criterion:

256

$$257 \quad \eta = \eta_{\text{creep}}, \text{ when } 2\dot{\epsilon}_{\text{II}}\eta_{\text{creep}} < \sigma_{\text{yield}}, \quad (4a)$$

$$258 \quad \eta = \eta_{\text{MC}}, \text{ when } 2\dot{\epsilon}_{\text{II}}\eta_{\text{creep}} > \sigma_{\text{yield}}, \quad (4b)$$

259

260 where  $\eta_{\text{creep}}$  is the creep viscosity. The creep viscosity, depending on the stress and  
261 temperature, is defined by the following power law equation:

262

$$263 \quad \eta_{\text{creep}} = 1/2\dot{\epsilon}_{\text{II}}^{(1-n)/n} A^{-1/n} \exp(E/nRT), \quad (5)$$

264

265 where  $A$  is the pre-exponential factor [ $\text{Pa}^n \cdot \text{s}$ ],  $E$  is the activation energy [ $\text{J/mol}$ ],  $n$  is  
266 the stress exponent,  $T$  is the temperature [ $\text{K}$ ], and  $R$  is the gas constant ( $8.314$   
267  $\text{J}/(\text{K} \cdot \text{mol})$ ).

268 In this study, for the sediment layer and the upper basement layer (i.e., the upper  
269 crust), we used the flow law parameters for wet quartz ( $A = 4.0 \times 10^{-11.2}/(\text{MPa}^n \cdot \text{s})$ ,  
270 including the effect of a constant water fugacity of 4 MPa at  $T = 473 \text{ K}$  and  $P = 200$

271 MPa,  $n = 4$ , and  $E = 135$  kJ/mol; Hirth et al. 2001), and for the lower basement layer  
272 (i.e., the lower crust), we used the flow law parameters for wet plagioclase ( $An_{60}$ ) ( $A =$   
273  $1.0 \times 10^{-1.5}/(\text{MPa}^n \cdot \text{s})$ ,  $n = 3$ , and  $E = 235$  kJ/mol; Rybacki and Dresen 2004). To  
274 incorporate the effect of strain weakening, it is modelled as a linear decrease of friction  
275 angle and cohesion between accumulated strain of  $\varepsilon_{II} = 0$  and  $\varepsilon_{II} = 1$ . These lower and  
276 upper thresholds of strain for weakening activation and completion are similar to those  
277 in previous numerical investigations of strain weakening of crustal rocks (e.g., Allken et  
278 al 2012; Ruh et al. 2014; Döhmann et al. 2019). At  $\varepsilon_{II} < 1$ , the cohesion and friction  
279 angle change linearly from the initial cohesion ( $C_i$ ) and initial friction angle ( $\varphi_i$ ) to the  
280 weakened cohesion ( $C_w$ ) and weakened friction angle ( $\varphi_w$ ), respectively, whereas at  $\varepsilon_{II}$   
281  $\geq 1$ , the cohesion and friction angle are constant at  $C_w$  and  $\varphi_w$ . For the basement layer,  $C_i$   
282 and  $C_w$  are  $10^7$  Pa and  $10^6$  Pa, respectively, and  $\varphi_i$  and  $\varphi_w$  are  $44^\circ$  (initial friction  
283 coefficient  $\mu_i = \sim 0.7$ ) and  $30^\circ$  (weakened friction coefficient  $\mu_w = \sim 0.5$ ), respectively.  
284 The value of the weakened friction coefficient corresponds to the experimentally  
285 determined values for phyllosilicate minerals, i.e., mica and chlorite (Morrow et al.  
286 2000; Ikari et al. 2011), and the value for damage zones of the San Andreas fault

287 (Carpenter et al. 2015). For the sediment layer, according to Gerya et al. (2009) and  
288 Gerya (2010), the physical properties of  $C_i = C_w = 10^6$  Pa,  $\varphi_i = 14^\circ$ , and  $\varphi_w = 6^\circ$  are  
289 employed for the calculation. The shear modulus  $G$  of the upper basement layer and the  
290 sediment layer is  $1.0 \times 10^{10}$  Pa, and that of the lower basement layer is  $2.5 \times 10^{10}$  Pa.

291 An energy conservation law that does not consider internal heat generation can be  
292 expressed as

293

$$294 \quad \rho C_p \frac{DT}{Dt} = \frac{\partial q_x}{\partial x} + \frac{\partial q_z}{\partial z}, \quad (6a)$$

$$295 \quad q_x = k \frac{\partial T}{\partial x}, \quad q_z = k \frac{\partial T}{\partial z}, \quad (6b)$$

296

297 where  $q_x$  and  $q_z$  are the conductive heat fluxes in the horizontal and vertical directions,  
298 respectively,  $t$  is time [s],  $\rho$  is the local density depending on the composition,  $C_p$  is the  
299 specific heat at constant pressure, and  $k$  is the thermal conductivity. According to Gerya  
300 et al. (2009) and Gerya (2010), the values of  $C_p$  for the sedimentary layer and the  
301 basement are set to 1,000 J/(kg·K) and the value of  $k$  [W/(m·K)] for the sedimentary  
302 layer and the upper basement is  $0.64 + 807/(T + 77)$  while that for the lower basement is

303  $1.18 + 474/(T + 77)$ .

304 Conservation of mass is approximated by the incompressible time-dependent  
305 two-dimensional continuity equation:

306

$$307 \quad \frac{\partial v_x}{\partial x} + \frac{\partial v_z}{\partial z} = 0, \quad (7)$$

308

309 where  $v_x$  and  $v_z$  are the horizontal and vertical components of the velocity vector,  
310 respectively.

311 The two-dimensional Stokes equations for creeping flow are

312

$$313 \quad \frac{\partial \sigma_{xx}}{\partial x} + \frac{\partial \sigma_{xz}}{\partial z} = \frac{\partial P}{\partial x}, \quad (8a)$$

$$314 \quad \frac{\partial \sigma_{zx}}{\partial x} + \frac{\partial \sigma_{zz}}{\partial z} = \frac{\partial P}{\partial z} - \rho g, \quad (8b)$$

315

316 where  $g$  is the gravitational acceleration ( $9.81 \text{ m/s}^2$ ). In this study, the densities of the  
317 sediment, upper basement, and lower basement are  $2,600 \text{ kg/m}^3$ ,  $2,700 \text{ kg/m}^3$ , and  $2,800$   
318  $\text{kg/m}^3$ , respectively. A weak layer above the lithosphere (“sticky air”,  $\eta = 10^{18} \text{ Pa s}$ ,  $\rho =$

319  $1 \text{ kg/m}^3$ ,  $k = 300 \text{ W/(m}\cdot\text{K)}$ ,  $C_p = 3.0 \times 10^6 \text{ J/(kg}\cdot\text{K)}$ ) provides a free-surface-like  
320 condition, which is essential to transform crust or sediment naturally (Gerya and Yuen  
321 2003, 2007; Gerya 2010).

322 The calculation domain in the initial state was  $80 \text{ km} \times 35 \text{ km}$  (Fig. 4). The size of  
323 the basement layers was  $80 \text{ km} \times 30 \text{ km}$ . All models used a finite-difference with  
324 marker-in-cell technique and were conducted on a fully staggered rectangular Eulerian  
325 grid with 4,480,000 markers. The grid spacing was irregular and was initially applied as  
326 an  $800 \times 210$  grid of  $80 \text{ km} \times 21 \text{ km}$  in the upper domain and as an  $800 \times 60$  grid of  $80$   
327  $\text{km} \times 14 \text{ km}$  in the lower domain. The grid spacing was recalculated at each time step to  
328 accommodate the horizontal shortening described below. The initial position of each  
329 marker was evenly set and then given random noise using the MATLAB<sup>®</sup> random  
330 number generator and, in some cases, we changed the random seed to evaluate the  
331 effect of the initial position of the markers. The absolute time step was 10 kyr. The  
332 calculation time was set to 3 Myr according to the fission track age (2.71 million years  
333 ago; Itihara et al. 1984) of the volcanic ash layer at the bottom of the Osaka Group.

334 We applied free-slip conditions at all boundaries and constant leftward and

335 downward velocities at the right and bottom boundaries, respectively. Temperatures at  
336 the top and bottom boundaries were constant, i.e., 0 °C and 750 °C, respectively, and  
337 the right and left boundaries were adiabatic. An initial geothermal gradient of 25 °C/km  
338 (e.g., Okubo et al. 2005) was applied to the basement layer, whereas there was no  
339 temperature gradient in the sticky air layer (i.e., the temperature at the top of the  
340 basement layer was also 0 °C). Following the horizontal shortening strain rate ( $16\text{--}26 \times$   
341  $10^{-9}/\text{yr}$ ) for central Japan of Wesnousky et al. (1982), the horizontal shortening rate was  
342 set to 2 m/kyr (Fig. 4). Therefore, at the end of the calculation (3 Myr), the 80-km-wide  
343 crust was shortened by 6 km. To conserve mass in the calculation domain, a changing  
344 downward velocity (from 0.88 m/kyr at 0 Myr to 1.02 m/kyr at 3 Myr) was applied at  
345 the bottom boundary.

346 To model preexisting faults, strained zones with a strain,  $\epsilon_{II}$ , of 1, having the initial  
347  $C_w$  and  $\phi_w$ , and a yield stress or plastic strength weaker than the surrounding rock mass  
348 were applied in the basement layer as high-strained weak zones. In this study, we refer  
349 to such high-strained weak zones as “faults” or “fault zones”. Even though the width of  
350 a preexisting fault zone was set to 250 m, that is, 2.5 times wider than the grid space,

351 the width of the zone follows the scaling law of the linear relationship between the  
352 width of the fault process zone and the fault length with a proportionality constant on  
353 the order of  $10^{-2}$  (Vermilye and Scholz 1998).

354 To model sedimentation processes, we introduced an imposed sea level change that  
355 is consistent with the geologically observed sedimentation rate at the location of the  
356 OD-1 core site. At the initial state, the sea level was set to the boundary between the  
357 sticky air and the rock layer. At each time step, after all markers were moved according  
358 to the calculated velocity field, we changed the sea level and markers of the sticky air  
359 below the sea level were replaced with markers of the sedimentary layer. Surface  
360 erosion was not considered in this study.

361 We considered three types of cases with the simulation model: (1) cases without any  
362 preexisting fault zone; (2) cases with a single fault zone cutting the upper 12 km of the  
363 basement layer; and (3) cases with two preexisting fault zones corresponding to the  
364 Uemachi and Ikoma fault zones.

365

366 **Results and discussion**

367 Cases with no preexisting fault zone

368 In these cases, we did not consider sedimentation processes. In the cases without any  
369 preexisting fault, under the compressive stress field, the upper and lower basement  
370 layers deform homogeneously prior to 0.4–0.6 Myr, whereas after 0.4–0.6 Myr, in the  
371 upper basement layer, the strain is concentrated into narrow zones and localized  
372 high-strained zones, i.e., newly formed thrust faults that develop as a result of  
373 compression (Fig. 5). These cases demonstrate that simulation results with different  
374 random seeds at 3 Myr differ somewhat with respect to the dip directions of the newly  
375 formed thrust faults. The thrust faults grow downward from the surface because values  
376 of the yield stress  $\sigma_{\text{yield}}$  of a rock given by Eq. (3) are lower at shallower depths. They  
377 develop from the surface to the frictional–viscous transition zone, where the strain is  
378 accommodated primarily by frictional deformation with weakened friction ( $\mu_w$ ) relative  
379 to the viscous deformation (inset in Fig. 4). The dip angles of the faults are  $\sim 30^\circ$  near  
380 the surface but bend gently near the frictional–viscous transition depth. These fault  
381 geometries (i.e., dip angles of the faults) are not explicitly “determined” by the code but  
382 form spontaneously during the propagation of the high-strained zone involving markers

383 for which the yielding condition given by Eq. (3) is satisfied locally. When increasing  
384 the amount of horizontal shortening, the thickness of the early formed faults widens and  
385 becomes ~300–500 m at 3 Myr; however, the depth of the fault tips does not change  
386 significantly after ~2 Myr. In the lower basement layer, the strain is distributed to form  
387 large-scale folds instead of localized high-strained zones. The displacement along the  
388 faults leads to relative subsidence on the lower side of the faults or uplifting on the  
389 upper side. In general, the amount of vertical displacement decreases with distance from  
390 the faults. The blocks between faults with the same dip direction tilt antithetically (Fig.  
391 5a), whereas the blocks between faults with opposite dip directions rise or sink  
392 vertically (Fig. 5b).

393

394 Cases with a single preexisting fault zone

395 In these cases, we did not consider sedimentation processes. In the cases with a single  
396 fault zone, we set the fault to have different dip angles (i.e., 15°, 30°, 45°, and 60°) at  
397 the surface location of  $x = 23$  km. Based on the simulation results for the cases with no  
398 preexisting fault, because the local displacements in the strained zone in the deepest part

399 of the upper basement layer and the lower basement layer are negligible, we considered  
400 the faults as only preexisting above 12 km. In this case, the effect of changing the  
401 random seed is smaller than in the cases without a preexisting fault and we only show  
402 the results with the random seed = 1 in Fig. 6. In all the cases, at the initial stage, strain  
403 localization occurs in the preexisting fault zone. The zone widens and becomes a source  
404 for newly generated spray fault zones. Displacement occurs along the preexisting faults  
405 in the upper basement layer for dip angles of  $15^{\circ}$ – $45^{\circ}$  but not  $60^{\circ}$  (Fig. 6). When the dip  
406 angle of the preexisting fault is  $15^{\circ}$  or  $45^{\circ}$ , the displacement along the preexisting fault  
407 is relatively small and new high-strained zones with dip angles of  $\sim 30^{\circ}$  develop. The  
408 preexisting fault steepens by  $\sim 2^{\circ}$  because of the rotation of the fault during horizontal  
409 shortening. When the dip angle of the preexisting fault is  $30^{\circ}$ , which is suitable for  
410 horizontal compression, the displacement along the fault is significant and the fault  
411 ultimately steepens by  $\sim 10^{\circ}$  as a result of the horizontal shortening and the tilting of the  
412 upper basement layer. After the preexisting fault becomes steeper, new faults with dip  
413 angles of  $\sim 30^{\circ}$  are formed. Conversely, when the dip angle of the preexisting fault is  $60^{\circ}$ ,  
414 many new faults with dip angles of  $\sim 30^{\circ}$  are formed and evenly displaced; in this case,

415 the preexisting fault ultimately steepens by  $\sim 2^\circ$ .

416 When the faults contain large amounts of clay minerals, the experimentally derived  
417 friction coefficient for the fault zone decreases to  $\sim 0.1$ – $0.2$  (Takahashi et al. 2007; Ikari  
418 et al. 2011). In fact, the frictional strength estimated for the weakest section of the San  
419 Andreas fault is  $\sim 0.1$  but increases abruptly to a value of  $\sim 0.4$ – $0.5$  in the host  
420 sedimentary rocks (Carpenter et al. 2015). We performed a simulation for a single  
421 preexisting fault zone with lower friction values of  $\mu_w = \sim 0.4$  and  $\sim 0.3$  ( $\phi_w = 24^\circ$  and  
422  $17^\circ$ , respectively). Figure 7 shows the results of the effect of the different weakened  
423 friction values on the activity of a preexisting fault with a dip angle of  $60^\circ$ . In this case,  
424 the preexisting fault, which is not favorably oriented to the horizontal compressional  
425 stress field, is active under the condition of  $\mu_w < 0.4$ .

426

427 Cases with two preexisting fault zones

428 In these cases, we consider the sedimentation process. We set two faults, whose  
429 locations at the surface were  $x = 23$  km (i.e., the western fault) and  $x = 40$  km (i.e., the  
430 eastern fault). The western and eastern faults correspond to the Uemachi and Ikoma

431 faults, respectively, which are separated by ~14 km at the surface in the final state. At  
432 the location equivalent to  $x = 18$  km in the initial state, corresponding to the OD-1 core  
433 site, which is ~5 km west of the Uemachi fault, we set the mean sedimentation rate to  
434 deposit 900 m of the Miyakojima Formation and 650 m of the Tanaka and Namba  
435 formations (i.e., 0.5 m/kyr from 0 to 1.8 Myr, 0.6 m/kyr from 1.8 Myr to 2.6 Myr, and  
436 0.4 m/kyr from 2.6 Myr to 3.0 Myr). Because Quaternary sediments are basically absent  
437 in the Ikoma Mountains (with a highest elevation of 642 m), the Ikoma Mountains may  
438 have been separated from the marine waters at 3 million years ago (Ma). However,  
439 because the elevation of the Ikoma Mountains at 3 Ma is unknown, the elevation of the  
440 Ikoma Mountains was assumed to be 0 m at 3 Ma (at 0 Myr in this study). According to  
441 the results for the cases with a single fault zone (Fig. 6), the optimal dip angle for the  
442 resolved shear stress is  $\sim 30^\circ$  and the dip angles of the western and eastern faults should  
443 also be  $\sim 30^\circ$ . Based on the geological interpretation, because the vertical displacement  
444 rate related to the Ikoma fault has been estimated to be much higher than that related to  
445 the Uemachi fault (Table 1), the dip angle of the western fault was set to differ slightly  
446 from the optimal value for the resolved shear stress, or the friction coefficients for the

447 eastern fault were set to be lower than those for the western fault. Because previous  
448 studies have generally suggested that the dip angle of the Uemachi fault is steeper than  
449 that of the Ikoma fault (Fig. 1) and because the dip angle of the Uemachi fault was  
450 recently estimated to be  $\sim 40^\circ$  (Kato and Ueda 2019), we applied dip angles of  $40^\circ$  and  
451  $30^\circ$  to the western and eastern faults, respectively (Fig. 8a). In this case, the downward  
452 extension of the western fault nearly coincides with the epicenter of the 2018 northern  
453 Osaka earthquake.

454 We compared the simulation results and geologic structures proposed by Uchiyama  
455 et al. (2001, Fig. 3) based on the following points: (1) the large-scale variation in the  
456 thickness of the upper and uppermost sedimentary layers, corresponding to the Tanaka  
457 and Namba formations, in the area in-between the western and eastern faults, i.e., in east  
458 Osaka, especially at the location of the OD-9 core site ( $\sim 2$  km east from the Uemachi  
459 fault at the final state) in the Uemachi Upland and at the location of the OD-3 core site  
460 ( $\sim 9$  km east from the Uemachi fault at the final state) near the Onchi River, and (2) the  
461 vertical displacement rates after 1.8 Myr, corresponding to the sedimentation period of  
462 the Tanaka and Namba formations, estimated by the vertical differences between the

463 highest point of the hanging wall basement and the lowest point of the foot wall  
464 basement near the western and eastern faults.

465 The displacement along the western and eastern faults leads to relative subsidence on  
466 the lower side of the faults so that sediment layers form in the relative subsidence  
467 regions (Fig. 8a). The surface of the basement slopes to the east as a whole, and an  
468 eastward thickening of the sedimentary layers throughout the Osaka Plain is observed.  
469 These layers result from the displacement along the eastern fault being much larger than  
470 that along the western fault (Table 1). The region west of the eastern fault is tilted  
471 eastward as a whole, even though displacement along the western fault and a difference  
472 in the sedimentary layer thickness between the areas on both sides of the western fault  
473 are observed. As shown in Fig. 8b, the vertical displacement rates related to the western  
474 and eastern faults increase monotonically prior to  $\sim 0.5$  Myr. At the initial stage ( $< \sim 0.5$   
475 Myr) of the simulation, the deformation does not concentrate along the entire fault; the  
476 deformation front moves downward along the fault, and then the entire fault deforms  
477 after  $\sim 0.5$  Myr. Therefore, the monotonical increase in the displacement rate at the  
478 initial stage of the simulation results from the increase in the deforming length along the

479 faults. The vertical displacement rate related to the eastern fault increases to ~1 m/kyr at  
480 ~1 Myr and becomes stable, whereas that along the western fault increases to ~0.3  
481 m/kyr at ~0.5 Myr and then decreases. This implies that the deformation of the eastern  
482 fault is predominant after ~0.5 Myr, even though the deformation is more partitioned in  
483 the eastern fault, and then the western and eastern faults deform stably after ~1 Myr.  
484 The mean vertical displacement rates along the western and eastern faults for the last 1  
485 Myr are ~0.07 m/kyr and ~0.8 m/kyr, respectively (Fig. 8b and Table 1). The mean  
486 displacement rate along the western fault is much slower than the inferred displacement  
487 rate along the Uemachi fault (~0.3–0.4 mm/yr; Uchiyama et al. 2001; Headquarters for  
488 Earthquake Research Promotion of MEXT 2001), whereas that along the eastern fault  
489 corresponds to the inferred displacement rate along the Ikoma fault (0.5–1 m/kyr;  
490 Shimokawa et al. 1997).

491 The depth of the basement surface is approximately 1,400 m at the location of the  
492 OD-9 core site in the Uemachi Upland and approximately 1,900 m at the location of the  
493 OD-3 core site near the Onchi River (Table 1). Both results are deeper than the  
494 geologically inferred values. The thickness of the sediment layer, corresponding to the

495 Tanaka and Namba formations, increases eastward; it is ~690-m thick near the Uemachi  
496 Upland and ~870-m thick near the Onchi River. Both results are thicker than the  
497 geologically inferred value. The sedimentation rate near the Onchi River is 0.7 m/kyr  
498 for the period of 1.8–2.4 Myr, corresponding to the lower Tanaka Formation, whereas  
499 that near the Uemachi Upland is 0.6 m/kyr for the same period (Fig. 8c); the former is  
500 consistent with geologically inferred values, but the latter is faster than the geologically  
501 inferred values (Table 1). However, although the sedimentation rate near the Onchi  
502 River hardly changes from 1.8 Myr to 2.4 Myr, the geologically inferred sedimentation  
503 rate decreases from 1.2 Ma to 0.6 Ma (Uchiyama et al. 2001). Consequently, in this case,  
504 the thicknesses of the upper and uppermost sedimentary layers corresponding to the  
505 lower Tanaka Formation and the upper Tanaka and Namba formations near the Uemachi  
506 Upland differ from the geological interpretation by ~160 m and ~280 m, respectively.  
507 The mean displacement rate along the western fault is smaller than that inferred from  
508 the geological observations. To resolve this discrepancy, the displacement rate along the  
509 western fault needs to be enhanced by decreasing the dip angle of the fault at least  
510 partially and/or by decreasing the friction coefficients. Accordingly, we evaluated

511 gentler ( $30^\circ$ ) or curved western fault cases (Fig. 9). In the curved fault cases, the dip  
512 angle of the western fault is  $40^\circ$  at the surface and gradually decreases with depth. The  
513 dip angle of the deeper part ( $>7$  km) of the western fault is constant and is  $20^\circ$  in the  
514 curved fault case and  $15^\circ$  in the more curved fault case.

515 Figure 9a illustrates the results of the case with the gentler dip angle ( $30^\circ$ ) for the  
516 western fault (the gentler Uemachi case). The displacement rate along the western fault  
517 is much higher than that in the case with the dip angle of the western fault set to  $40^\circ$ ,  
518 whereas the displacement rate along the eastern fault is lower, implying that more  
519 deformation is partitioned to the western fault, decreasing the displacement rate along  
520 the eastern fault. Although the dip angle of the both faults is the same, the displacement  
521 rate along the western fault is lower than that along the eastern fault. It may be resulted  
522 from the effects of viscous flow near the bottom of the lower basement layer; when the  
523 adjacent, parallel preexisting faults are eastward dipping, the downward extension of the  
524 easternmost fault (i.e., the eastern fault in this case) develops as a lower crustal  
525 high-strained zone connecting to the basal viscous flow and then the strain localizes into  
526 the eastern fault (Additional file 1: Fig. S1). The eastern fault and its downward

527 extension act as a bounding fault between the less deformed hanging wall and footwall  
528 blocks. A local uplift of the high-strained triangular zone of the sedimentary layers in  
529 between conjugate fault set propagated from the tip of the western fault is observed. The  
530 formation of the conjugate fault set may be resulted from the increase in the  
531 displacement rate and/or the decrease in the dip angle of the western fault. Based on a  
532 comparison with the geological interpretation, this gentler Uemachi case is more  
533 suitable; however, the difference between the geological interpretation and the  
534 simulation results is still large, especially the thickness of the uppermost sedimentary  
535 layer in the Uemachi Upland and the basement depth near the Onchi River (Table 1).

536 The results of the curved fault cases (the curved and more curved Uemachi cases) are  
537 illustrated in Fig. 9b–e. Nearly horizontal sedimentary layers form in west Osaka,  
538 whereas an eastward thickening of the sedimentary layers is observed in east Osaka.  
539 The surface of the basement in east Osaka slopes to the east, whereas that in west Osaka  
540 is nearly horizontal. These slopes result from the clockwise rotation of the east Osaka  
541 block arising from the displacement along the synthetic eastern and western faults. The  
542 degree of tilting toward the east of the east Osaka block in the curved western fault

543 cases is larger than that in the non-curved cases; however, the difference in the degree of  
544 tilting between the curved and more curved cases is not significant. The thickness of the  
545 sediment layer in east Osaka in the more curved western fault case is larger than that in  
546 the less curved case (Table 1). Based on a comparison with the geological interpretation,  
547 the less curved case is the more suitable geometry for the present numerical model. In  
548 the curved fault case, the numerical results are consistent with the geological  
549 interpretation, even though the thickness of the uppermost sedimentary layer near the  
550 Uemachi Upland differs from the geological interpretation by ~170 m. This difference  
551 may be reduced by a higher vertical displacement rate along a fine-tuned, optimally  
552 curved western fault.

553 The difference in the thickness of the uppermost sedimentary layer between the  
554 simulation results and the geological interpretation may also be due to the effect of the  
555 changing sedimentation rate for the uppermost sedimentary layer. In this study, we set  
556 the mean sedimentation rate at the OD-1 core site to 0.4 m/kyr from 2.6 Myr to 3.0 Myr,  
557 even though the sedimentation rate from ~0.4 Ma to ~0.05 Ma actually decreased from  
558 0.5 m/kyr to 0.2 m/kyr (Uchiyama et al. 2001). Furthermore, in the present simulation

559 models, the subsidence rate in west Osaka decreases with distance from the western  
560 fault, even though, based on gravity and seismic reflection data (e.g., Nakagawa et al.  
561 1996b; Iwabuchi 2000), the top of the basement deepens toward the west and the  
562 deepest part of the Osaka Bay is located ~27 km from the Uemachi fault, where the  
563 NNE–SSW-trending Osaka-wan fault is located. The Osaka-wan fault is an  
564 ESE-side-down reverse fault, having a mean vertical displacement rate of 0.5–0.6 m/kyr  
565 after 1 Ma (Yokokura et al. 1998). If the subsidence rate at the OD-1 site related to the  
566 activity of the Osaka-wan fault is higher than that used in the present models, the  
567 sedimentation rate in east Osaka will be lower because the rising rate of the sea level  
568 will be reduced. Further studies need to evaluate the effect of changing the  
569 sedimentation rate and vertical displacement along the Osaka-wan fault on the  
570 development of the geologic structures of the upper and uppermost sedimentary layers.

571

572 Evaluation of previously proposed fault geometry models

573 As previously mentioned, geometries of the deeper parts of the Uemachi and Ikoma  
574 faults have been proposed by Ishiyama (2003) and Sato et al. (2009). In this section, we

575 evaluate their proposed Uemachi and Ikoma fault geometries.

576 Following Ishiyama (2003), we applied two faults initially in the basement layer with  
577 the western and eastern faults corresponding to the Uemachi and Ikoma faults,  
578 respectively (Fig. 10a). The dip angles of the western and eastern faults near the surface  
579 were  $40^\circ$  and  $55^\circ$ , respectively. The surface positions of the two faults were the same as  
580 in the cases with two preexisting fault zones. The eastern fault was linear, whereas the  
581 western fault had a downward convex curving part at a depth of  $\geq 1.5$  km, became nearly  
582 horizontal ( $2^\circ$ ) at a depth of 3.5 km, and then converged to the eastern fault at a depth of  
583  $\sim 4$  km. Because a preexisting weak fault with a dip angle of  $\sim 60^\circ$  is active when the  
584 weakened friction coefficient ( $\mu_w$ ) is less than  $\sim 0.3$ , we performed numerical  
585 simulations for this case with  $\mu_w = 0.3$ . In this case, even though the eastern fault (dip  
586 angle of  $55^\circ$ ) was active, displacement related to the western fault (dip angle of  $40^\circ$ ) is  
587 not significant and does not occur along the deeper ( $> 3.5$  km) and horizontal ( $< 2^\circ$ ) parts  
588 of the fault. A newly formed fault with a dip angle of  $\sim 30^\circ$  propagates from the  
589 shallower and steeper parts of the western fault, and displacement related to the  
590 Uemachi fault occurs along this newly formed fault. This result implies that a

591 thin-skinned thrust converging to a low-angle detachment in the upper crust would not  
592 be active. The displacement along the eastern fault is significant but a large-scale  
593 downward fold, i.e., synform, is formed in the area east to the eastern fault, leading to  
594 the development of a sedimentary basin.

595 According to Sato et al. (2009), the western fault has a near surface dip angle of  $50^\circ$ ,  
596 transitions to gently dipping at a depth of  $\leq 7$  km, and then converges to the eastern fault  
597 at a depth of  $\sim 9$  km (Fig. 10b) with a dip angle of  $4^\circ$ . The dip angle of the eastern fault  
598 near the surface was set to  $45^\circ$ , and the eastern fault transitioned to gently dipping at a  
599 depth of 5 km. Below the converged depth, the dip angle of the eastern fault was set to  
600  $20^\circ$ . The surface positions of the two faults were the same as in the cases with two  
601 preexisting fault zones. We performed numerical simulations for this case with  $\mu_w = 0.4$ .  
602 The simulation results are similar to the curved Uemachi case (Figs. 9b and 10b), which  
603 correspond roughly to the geological interpretation (Table 1). The displacements along  
604 the lower ( $>9$  km) and horizontal ( $<4^\circ$ ) parts of the Uemachi fault are not significant,  
605 and the newly formed high-strained zones with a dip angle of  $\sim 30^\circ$  propagate from the  
606 upper bound of the lower and horizontal parts (Additional file 1: Fig. S2). Therefore, the

607 actual fault geometry of this model is similar to our curved Uemachi case at shallower  
608 depths (<~10 km).

609

### 610 **Concluding remarks**

611 Based on a simple numerical analysis, we can conclude that, when the friction  
612 coefficient of the faults is approximately 0.5, the dip angles of the Uemachi and Ikoma  
613 faults near the surface are ~30°–40° and the Uemachi fault has a downward convex  
614 curve at the bottom of the seismogenic zone but does not converge to the Ikoma fault.  
615 This implies that the downward extension of the Uemachi fault zone nearly coincides  
616 with the epicenter of the 2018 northern Osaka earthquake.

617

### 618 **Abbreviations**

619 MEXT: Ministry of Education, Culture, Sports, Science and Technology of Japan.

620

### 621 **Author's contributions**

622 HN, TO and KI performed the numerical simulations and evaluated the model results.

623 MM evaluated the geological features in the Osaka Plain to constrain the model  
624 results. HN and TO drafted mainly the manuscript, and all authors read and approved  
625 the final manuscript.

626

### 627 **Acknowledgements**

628 We thank TV Gerya for his providing the I2ELVIS code via the Cambridge University  
629 Press website (<https://www.cambridge.org/9780521887540>).

630

### 631 **Competing interests**

632 The authors declare that they have no competing interests.

633

### 634 **Availability of data and materials**

635 All data generated or analyzed during this study are available from the corresponding  
636 author on reasonable request.

637

### 638 **Consent for publication**

639 Not applicable.

640

641 **Funding**

642 This study supported by JSPS KAKENHI Grant Number 20K04087.

643

644 **References**

645 Allken V, Huismans RS, Thieulot C (2012) Factors controlling the mode of rift

646 interaction in brittle-ductile coupled systems: A 3D numerical study. *Geochem*

647 *Geophys Geosystem* 13, Q05010. <https://doi.org/10.1029/2012GC004077>

648 Allmendinger RW (1998) Inverse and forward numerical modeling of trishear

649 fault-propagation folds. *Tectonics* 17:640–656

650 Carpenter BM, Saffer DM, Marone C (2015) Frictional properties of the active San

651 Andreas Fault at SAFOD: Implications for fault strength and slip behavior. *J*

652 *Geophys Res* 120:5273–5289. <https://doi.org/10.1002/2015JB011963>

653 Director General for Disaster Management (2006) Evaluation of inundation possibility

654 associated with crustal deformation due to earthquake in the Uemachi fault zone.

655 [http://www.bousai.go.jp/kaigirep/chuobou/senmon/tounankai\\_nankaijishin/pdf/2\\_](http://www.bousai.go.jp/kaigirep/chuobou/senmon/tounankai_nankaijishin/pdf/2_)  
656 [kohyo.pdf](#). Accessed 10 Sept 2020

657 Döhmann MJE, Brune S, Nardini L, Rybacki E, Dresen G (2019) Strain localization and  
658 weakening processes in viscously deforming rocks: Numerical modeling based on  
659 laboratory torsion experiments. *J Geophys Res: Solid Earth* 124:1120–1137.  
660 <https://doi.org/10.1029/2018JB016917>

661 Gerya T (2010) *Introduction to Numerical Dynamic Modelling*. Cambridge Univ Press,  
662 New York

663 Gerya TV, Yuen DA (2003) Rayleigh–Taylor instabilities from hydration and melting  
664 propel 'cold plumes' at subduction zones. *Earth Planet Sci Lett* 212:47–62.  
665 [https://doi.org/10.1016/S0012-821X\(03\)00265-6](https://doi.org/10.1016/S0012-821X(03)00265-6)

666 Gerya TV, Yuen DA (2007) Robust characteristics method for modelling multiphase  
667 visco-elasto-plastic thermo-mechanical problems. *Phys Earth Planet Int* 163:83–105.  
668 <https://doi.org/10.1016/j.pepi.2007.04.015>

669 Gerya TV, Fossati D, Cantieni C, Seward D (2009) Dynamic effects of aseismic ridge  
670 subduction: numerical modelling. *Eur J Mineral* 21:649–661.

671 <https://doi.org/10.1127/0935-1221/2009/0021-1931>

672 Headquarters for Earthquake Research Promotion of MEXT (2001) Long-term  
673 evaluation of Ikoma fault zone.  
674 [http://www.jishin.go.jp/main/chousa/katsudansou\\_pdf/77\\_ikoma.pdf](http://www.jishin.go.jp/main/chousa/katsudansou_pdf/77_ikoma.pdf). Accessed 10  
675 Sept 2020

676 Headquarters for Earthquake Research Promotion of MEXT (2004) Long-term  
677 evaluation of Uemachi fault zone.  
678 [http://www.jishin.go.jp/main/chousa/katsudansou\\_pdf/80\\_uemachi.pdf](http://www.jishin.go.jp/main/chousa/katsudansou_pdf/80_uemachi.pdf). Accessed  
679 10 Sept 2020

680 Horike M, Takeuchi Y, Toriumi I, Fujita T, Yokota H, Noda T (1995) Seismic reflection  
681 survey of the boundary region between the Ikoma mountains and the Osaka basin.  
682 *Zisin* 48:37–49

683 Huzita K (1968) Rokko movements and its appearance –Intersecting structural  
684 patterns of southwest Japan and Quaternary crustal movements–. *Quaternary Res*  
685 (Daiyonki-Kenkyu) 7:248–260

686 Huzita K (1990) Manchidani Unconformity and Rokko movements –Middle

687 Pleistocene fault-block movement and sea-level rise in Kinki, Japan Quaternary Res  
688 (Daiyonki-Kenkyu) 29:337–349

689 Huzita K, Kasama T (1982) Geology of the Osaka-Seinambu district, Quadrangle Series,  
690 scale 1:50,000, Geological Survey of Japan, Tsukuba

691 Ikari MJ, Marone C, Saffer DM (2011) On the relation between fault strength and  
692 frictional stability. *Geology* 39:83–86. <https://doi.org/10.1130/G31416.1>

693 Ikebe N, Huzita K (1966) The Rokko movements, the Pliocene–Pleistocene crustal  
694 movements in Japan. *Quaternaria* 8:277–287

695 Ikebe N, Iwatsu J, Takenaka J (1970) Quaternary geology of Osaka with special  
696 reference to land subsidence. *J Geosci Osaka City Univ* 13:39–98

697 Ishiyama T (2003) Geometry and kinematics of the Uemachi and Ikoma fault zones  
698 beneath Metropolitan Osaka, central Japan. *Ann Rep Active Fault Paleoeearthquake*  
699 *Res*, no.3, p.145–155

700 Itihara M (1993) *Osaka Group*. Sogensha Publishing, Osaka

701 Itihara M, Yoshikawa S, Kawabe T, Mitamura M (1984) On so-called "Shiba  
702 Unconformity" in the drainage area of the River Tsuda, Kishiwada City, Osaka –

703 Magnetostratigraphy and fission track age of the Osaka Group-. Earth Sci  
704 (Chikyu-Kagaku) 38:1–16

705 Itoh Y, Takemura K, Ishiyama T, Tanaka Y, Iwaki H (2000) Basin formation at a  
706 contractional bend of a large transcurrent fault: Plio-Pleistocene subsidence of the  
707 Kobe and northern Osaka Basin, Japan. Tectonophysics 321:327–341

708 Iwabuchi Y (2000) Active structures in Osaka Bay and Ise Bay. Quaternary Res  
709 (Daiyonki-Kenkyu) 39:303–314

710 Iwasaki Y (2016) Fundamental mistake for estimation of the strong ground motion  
711 and displacements from Uemachi fault earthquake by the Central Disaster  
712 Management Council of the Cabinet Office, Government of Japan. Geoinformatics  
713 27:66–69

714 Kansai Geo-informatics Council (1998) New Kansai-jiban, Kobe and Hanshin Regions.  
715 Kansai Geoinformatics Agency/Geo-Research Institute, Osaka

716 Kato A, Ueda T (2019) Source fault model of the 2018  $M_W$  5.6 northern Osaka  
717 earthquake, Japan, inferred from the aftershock sequence. Earth Planets Space  
718 71:11. <https://doi.org/10.1186/s40623-019-0995-9>

- 719 Mitamura M, Matsuyama N, Nakagawa K, Yamamoto K, Suwa S (1994) Stratigraphy  
720 and subsurface structure of Holocene deposits around Uemachi Upland in the  
721 central Osaka Plain. *J Geosci Osaka City Univ* 37:183–212
- 722 Morrow CA, Moore DE, Lockner DA (2000) The effect of mineral bond strength and  
723 adsorbed water on fault gouge frictional strength. *Geophys Res Lett* 27:815–818
- 724 Nakagawa K, Inoue N, Ryoki K (1996a) Basement structure of Osaka basin. *Urban*  
725 *Earthquake Hazard Res Center Rep*, no. 18, p.11–25
- 726 Nakagawa K, Shiono K, Inoue N, Sano M (1996b) Geological characteristics and  
727 problems in and around Osaka Basin as a basis for assessment of seismic hazard.  
728 *Soils and Foundations* 36 (Supplement):15–28.  
729 [https://doi.org/10.3208/sandf.36.Special\\_15](https://doi.org/10.3208/sandf.36.Special_15)
- 730 Nakata T, Okada A, Suzuki Y, Watanabe M, Ikeda Y (1996a) 1:25,000-scale Active Fault  
731 Map in Urban Area, Osaka Tohoku-bu. *Technical Materials of the Geographical*  
732 *Survey Institute*, D.1-no. 333
- 733 Nakata T, Okada A, Suzuki Y, Watanabe M, Ikeda Y (1996b) 1:25,000-scale Active Fault  
734 Map in Urban Area, Osaka Tonan-bu. *Technical Materials of the Geographical*

- 735 Survey Institute, D.1-no. 333
- 736 Okada A, Togo M (2000) Active Faults in the Kinki Area, Central Japan: Sheet Maps and  
737 Inventories. Univ Tokyo Press, Tokyo
- 738 Okada A, Yagi, H (2019) Illustrated Active faults in Japan. Asakurashoten Publishing,  
739 Tokyo
- 740 Okada A, Uemura Y, Togo M, Nakata T, Watanabe M (1996) 1:25,000-scale Active Fault  
741 Map in Urban Area, Kyoto Seinan-bu. Technical Materials of the Geographical  
742 Survey Institute, D.1-no. 333
- 743 Okubo Y, Uchida Y, Taniguchi M, Miyakoshi A, Safanda J (2005) Statistical analysis for  
744 thermal data in the Japanese Islands. *Phys Earth Planet Inter* 152:277–291.  
745 <http://doi.org/10.1016/j.pepi.2005.04.013>
- 746 Osaka Prefecture (2004) Survey for the underground structure in the Osaka Plain.  
747 Report for basic earthquake-related survey grant FY2003, Osaka
- 748 Ruh JB, Gerya T, Burg JP (2014) 3D effects of strain vs. velocity weakening on  
749 deformation patterns in accretionary wedges. *Tectonophysics* 615–616:121–141.  
750 <http://dx.doi.org/10.1016/j.tecto.2014.01.003>

751 Sato H, Ito K, Abe S, Kato N, Iwasaki T, Hirata N, Ikawa T, Kawanaka T (2009) Deep  
752 seismic reflection profiling across active reverse faults in the Kinki Triangle, central  
753 Japan. *Tectonophysics* 472:86–94. <https://doi.org/10.1016/j.tecto.2008.06.014>

754 Shimokawa K, Kariya Y, Miyachi Y, Sangawa A (1997) Survey for the activity of the  
755 Ikoma fault system. *GSJ Open-file Rep*, no. 303, p.37–49

756 Sugiyama Y (1997) Seismic reflection survey of the Uemachi fault system. *GSJ*  
757 *Open-file Rep*, no. 303, p.105–113

758 Sugiyama Y, Sangawa A (1996) Seismic reflection survey of the southward extension  
759 of the Uemachi fault in the Yamato River, southern Osaka Plain. *GSJ Interim Rep*, no.  
760 EQ/96/1, p.57–62

761 Sugiyama Y, Shimokawa K, Awata Y, Satake K, Mizuno K, Yoshioka T, Komatsubara T,  
762 Nanayama F, Kariya Y, Azuma T, Fusejima Y, Tsukuda E, Sangawa A, Sugai T (1999)  
763 Summarized survey result and earthquake potential of major active faults in the  
764 Kinki Triangle, central Japan. *GSJ Interim Rep*, no. EQ/99/3, p.285–309

765 Sugiyama Y, Nanayama F, Kitada N, Yokota H (2001) S-wave seismic reflection survey  
766 of the Uemachi fault in Osaka City. *Ann Rep Active Fault Paleoequake Res*, no.

767 1, p.143–151

768 Sugiyama Y, Nanayama F, Miura K, Yoshikawa T, Yokota H, Suehiro M, Furutani M,  
769 Tochimoto Y, Hirose K, Yokoyama Y, Kitada N, Takemura K (2003) Complementary  
770 study of the Uemachi fault system in the Osaka Basin (2) –Evaluation of the fault  
771 activity based on supplementary boring and re-interpretation of S-wave seismic  
772 reflection data–. Ann Rep Active Fault Paleoequake Res, no. 3, p.117–144

773 Suzuki K (2016) Sedimentation rate and sedimentary process of the lower half of the  
774 Lower part of the Osaka Group, central Japan. J Sediment Soc Japan 75:25–34

775 Takahashi M, Mizoguchi K, Kitamura K, Masuda K (2007) Effects of clay content on  
776 the frictional strength and fluid transport property of faults. J Geophys Res  
777 112:B08206. <https://doi.org/10.1029/2006JB004678>

778 Terakawa T, Matsu'ura M (2010) The 3-D tectonic stress fields in and around Japan  
779 inverted from centroid moment tensor data of seismic events. Tectonics  
780 29:TC6008. <https://doi.org/10.1029/2009TC002626>

781 Tsukahara H, Kobayashi Y (1991) Crustal stress in the central and western parts of  
782 Honshu, Japan. Zisin 44:221–231

783 Tsutsumi H, Sato K, Yamaji A (2012) Stability of the regional stress field in central  
784 Japan during the late Quaternary inferred from the stress inversion of the active  
785 fault data. *Geophys Res Lett* 39:L23303. <https://doi.org/10.1029/2012GL054094>

786 Uchiyama M, Mitamura M, Yoshikawa S (2001) Displacement rate of the Uemachi  
787 Fault and basement block movements of the Osaka Plain, Southwest Japan. *J Geol  
788 Soc Japan* 107:228–236

789 Vermilye JM, Scholz CH (1998) The process zone: A microstructural view of fault  
790 growth. *J Geophys Res* 103:12223–12237

791 Wesnousky SG, Scholz CH, Shimazaki K (1982) Deformation of an island arc: Rates of  
792 moment release and crustal shortening in intraplate Japan determined from  
793 seismicity and Quaternary fault data. *J Geophys Res* 87:6829–6852

794 Yokokura T, Kano N, Yamaguchi K, Miyazaki T, Ikawa T, Ohta Y, Kawanaka T, Abe S  
795 (1998) Seismic profiling of deep geological structure in the Osaka Bay area. *Bull  
796 Geol Surv Japan* 49:571–590

797 Yoshikawa S, Mitamura M (1999) Quaternary stratigraphy of the Osaka Plain, central  
798 Japan and its correlation with oxygen isotope record from deep sea cores. *J Geol*

- 799 Soc Japan 105:332–340
- 800 Yoshikawa S, Machida Y, Teramoto M, Yokota H, Nagao H, Kagiwara M (1987)
- 801 Reflection seismic survey in Osaka City. Proc 77th SEGJ Conf, p.114–117
- 802 Yoshikawa S, Mizuno K, Katoh S, Satoguchi Y, Miyakawa C, Kinugasa Y, Mitamura M,
- 803 Nakagawa K (2000) Stratigraphy and correlation of the Plio-Pleistocene volcanic
- 804 ash layers from a 1,700 m core taken from Higashinada, Kobe City, southwestern
- 805 Japan. Quaternary Res (Daiyonki-Kenkyu) 39:505–520
- 806

807 **Figure legends**

808 **Fig. 1** Summary of the inferred geometries of the Uemachi and Ikoma faults in the  
809 Osaka Plain illustrated on a schematic geological cross section (modified partially  
810 from Ishiyama 2003). Here, references 1, 2, 3, 4, 5 and 6 correspond to Headquarters  
811 for Earthquake Research Promotion of MEXT (2001, 2004), Ishiyama (2003), Director  
812 General for Disaster Management (2006), Sato et al. (2009), Iwasaki (2016) and Kato  
813 and Ueda (2016), respectively. The epicenter of the 2018 northern Osaka earthquake  
814 (EQ) proposed by Kato and Ueda (2019), located 12 km beneath the surface position  
815 14 km from the Uemachi fault, is indicated by a star.

816 **Fig. 2 a** Locations of the drilling sites on the Osaka Plain referred to in this study.  
817 Faults and flexures of the Uemachi fault zone include the Uemachi fault (Um<sub>1</sub>),  
818 Sakuragawa flexure (Um<sub>2</sub>), Nagai fault (Um<sub>3</sub>), and Suminoe flexure (Um<sub>4</sub>), and those  
819 of the Ikoma fault zone include the Katano fault (Ik<sub>1</sub>), Hirakata fault (Ik<sub>2</sub>), and Ikoma  
820 fault (Ik<sub>3</sub>) (Headquarters for Earthquake Research Promotion of MEXT 2001, 2004).  
821 The inset indicates the location of the study area. **b** Columnar sections of the OD-1, TS,  
822 YU, OD-9, OT, OD-2, HA, and OD-3 drilling cores (partially modified from Uchiyama et

823 al. (2001)).

824 **Fig. 3** Schematic E–W geological section through the Osaka Plain (Uchiyama et al.  
825 2001).

826 **Fig. 4** Model geometry and boundary conditions. The inset shows the crustal strength  
827 profile at the initial state in the numerical model.  $\dot{\epsilon}$ ,  $\mu_i$  and  $\mu_w$  are the strain rate, the  
828 initial friction coefficient, and the weakened friction coefficient, respectively. A  
829 changing downward velocity (from 0.88 m/kyr at 0 Myr to 1.02 m/kyr at 3 Myr) is  
830 applied at the bottom boundary.

831 **Fig. 5** Results at 3 Myr for the numerical simulations with no preexisting fault zone.  
832 The newly formed faults (markers with a cumulative strain larger than 1) are illustrated  
833 in dark blue. **a** Case with the random seed number = 1. **b** Case with the random seed  
834 number = 3.

835 **Fig. 6** Results at 3 Myr for numerical simulations with a single preexisting fault zone.  
836 The preexisting fault (PF) and the newly formed faults (markers with a cumulative  
837 strain larger than 1) are illustrated in dark blue. The weakened friction coefficient  $\mu_w$  is  
838  $\sim 0.5$  (weakened friction angle  $\phi_w = 30^\circ$ ). **a** Case with a dip angle of  $15^\circ$ . **b** Case with a

839 dip angle of  $30^\circ$ . **c** Case with a dip angle of  $45^\circ$ . **d** Case with a dip angle of  $60^\circ$ .

840 **Fig. 7** Effect of different weakened friction coefficients  $\mu_w$  on the activity of a  
841 preexisting fault with a dip angle of  $60^\circ$ . **a** Case with  $\mu_w = \sim 0.4$  (weakened friction  
842 angle  $\phi_w = 24^\circ$ ). **b** Case with  $\mu_w = \sim 0.3$  ( $\phi_w = 17^\circ$ ). The preexisting fault (PF) and newly  
843 formed faults (markers with a cumulative strain larger than 1) are illustrated in dark  
844 blue.

845 **Fig. 8** Results of the numerical simulation for a case with two preexisting fault zones  
846 with dip angles of  $40^\circ$  and  $30^\circ$ , corresponding to the Uemachi and Ikoma faults in the  
847 Osaka Plain, respectively. **a** The initial model geometry and time evolution. The  
848 epicenter of the 2018 northern Osaka earthquake (Kato and Ueda 2019), located 12  
849 km beneath the surface position 14 km from the Uemachi fault, is indicated by a star.  
850 The lower panels show a close up view of a 60 km  $\times$  10 km domain including the  
851 western and eastern weak zones. The preexisting faults and newly formed faults  
852 (markers with a cumulative strain larger than 1) are illustrated in dark blue. **b** Time  
853 evolution of the vertical displacement rates along the western and eastern faults. **c**  
854 Time evolution of the sedimentation rates near the Uemachi Upland (i.e., at the

855 location of the OD-g core site) and the Onchi River (i.e., at the location of the OD-3  
856 core site). The imposed sedimentation rates at the location of the OD-1 core site are  
857 also shown.

858 **Fig. 9** Effect of changing the dip angle of the western fault (i.e., the Uemachi fault) on  
859 the development of the geologic structures. **a** The initial geometry (upper), final  
860 geometry (middle), and close up of the final geometry (lower) of the linear case with a  
861 dip angle of 30°. **b** The initial geometry (upper), final geometry (middle), and close up  
862 of the final geometry (lower) of the curved case. **c** The initial geometry (upper), final  
863 geometry (middle), and close up of the final geometry (lower) of the more curved case.  
864 The preexisting faults and newly formed faults (markers with a cumulative strain  
865 larger than 1) are illustrated in dark blue. The epicenter of the 2018 northern Osaka  
866 earthquake (Kato and Ueda 2019), located 12 km beneath the surface position 14 km  
867 from the Uemachi fault, is indicated by a star in the panels showing the result at 3 Myr.  
868 **d** Time evolution of the vertical displacement rates along the western and eastern  
869 faults for the curved case. **e** Time evolution of the sedimentation rates near the  
870 Uemachi Upland (i.e., at the location of the OD-g core site) and the Onchi River (i.e., at

871 the location of the OD-3 core site) for the curved case. The imposed sedimentation  
872 rates at the location of the OD-1 core site are also shown.

873 **Fig. 10** Results of the numerical simulations for previously proposed fault geometries.

874 **a** The initial geometry (upper), final geometry (middle), and close up of the final  
875 geometry (lower) for the fault geometry of Ishiyama (2003) with a weakened friction  
876 coefficient  $\mu_w$  of  $\sim 0.3$  (weakened friction angle  $\phi_w = 17^\circ$ ). **b** The initial geometry  
877 (upper), final geometry (middle), and close up of the final geometry (lower) for the  
878 fault geometry of Sato et al. (2009) with  $\mu_w = \sim 0.4$  ( $\phi_w = 24^\circ$ ). The preexisting faults  
879 and newly formed faults (markers with a cumulative strain larger than 1) are illustrated  
880 in dark blue. UmF and IkF represent the surface positions of the Uemachi and Ikoma  
881 faults, respectively.

# Figures

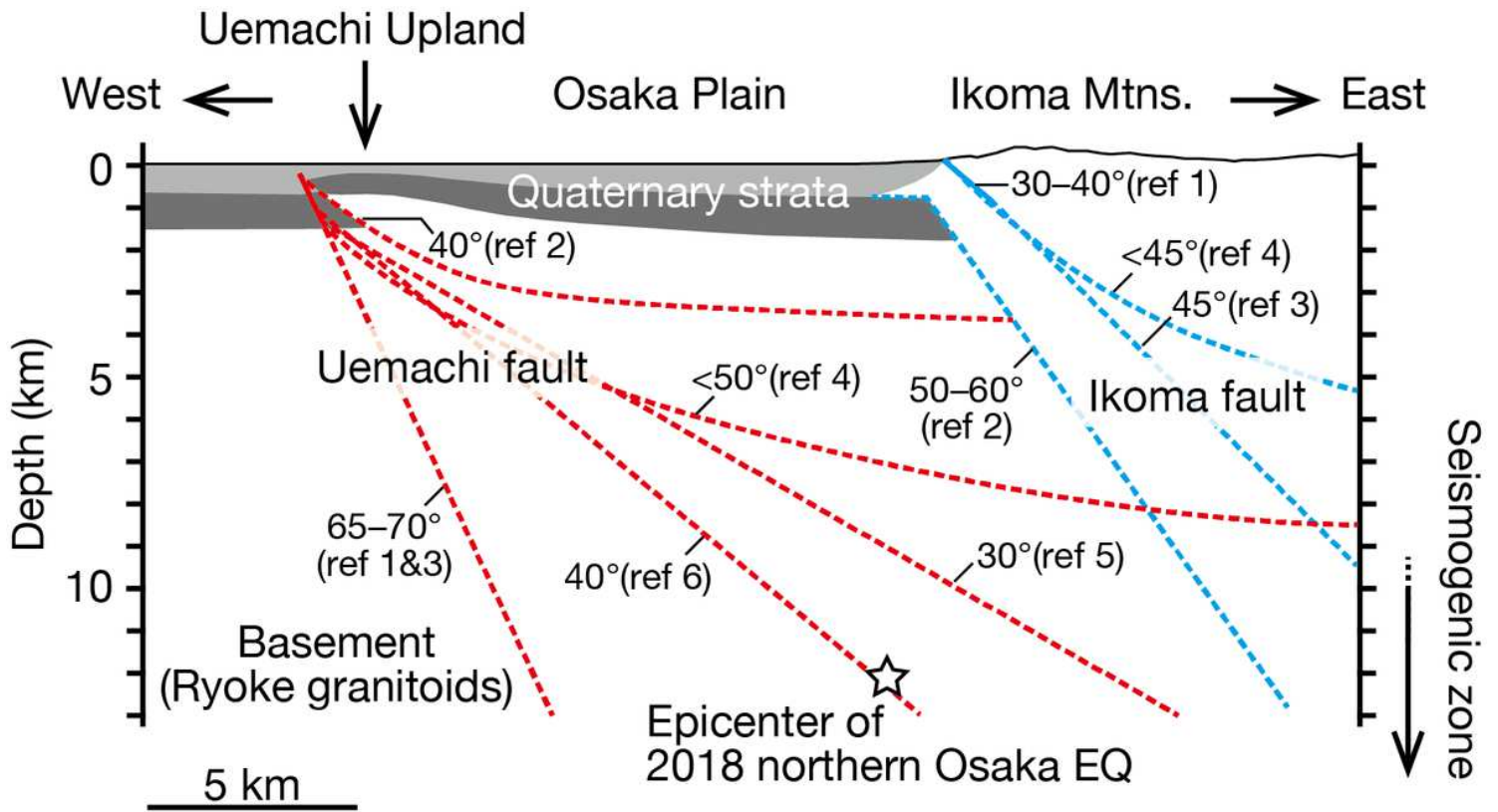


Figure 1

Figure 1

Summary of the inferred geometries of the Uemachi and Ikoma faults in the Osaka Plain illustrated on a schematic geological cross section (modified partially from Ishiyama 2003). Here, references 1, 2, 3, 4, 5 and 6 correspond to Headquarters for Earthquake Research Promotion of MEXT (2001, 2004), Ishiyama (2003), Director General for Disaster Management (2006), Sato et al. (2009), Iwasaki (2016) and Kato and Ueda (2016), respectively. The epicenter of the 2018 northern Osaka earthquake (EQ) proposed by Kato and Ueda (2019), located 12 km beneath the surface position 14 km from the Uemachi fault, is indicated by a star.

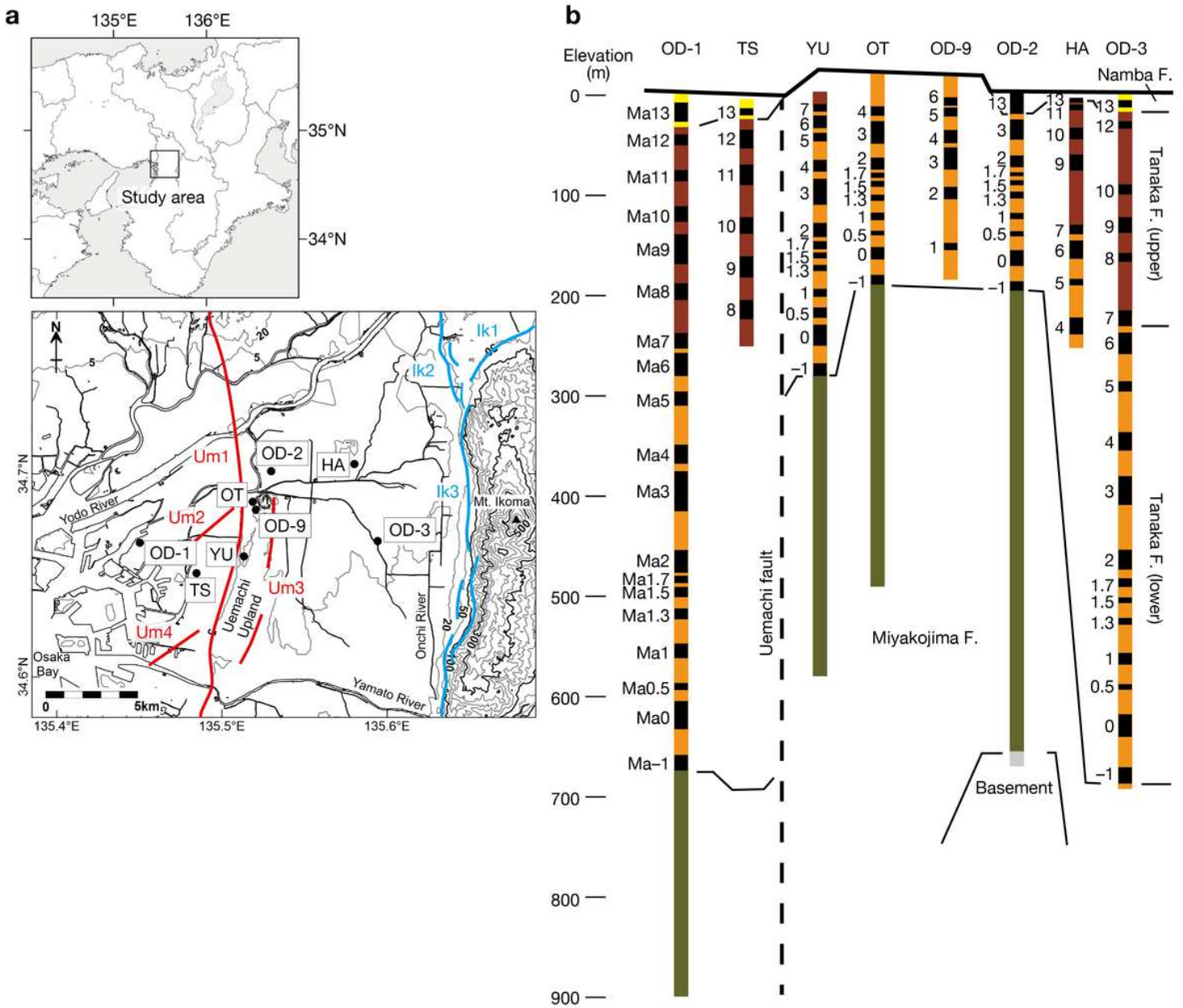


Figure 2

Figure 2

a Locations of the drilling sites on the Osaka Plain referred to in this study. Faults and flexures of the Uemachi fault zone include the Uemachi fault (Um1), Sakuragawa flexure (Um2), Nagai fault (Um3), and Suminoe flexure (Um4), and those of the Ikoma fault zone include the Katano fault (Ik1), Hirakata fault (Ik2), and Ikoma fault (Ik3) (Headquarters for Earthquake Research Promotion of MEXT 2001, 2004). The inset indicates the location of the study area. b Columnar sections of the OD-1, TS, YU, OD-9, OT, OD-2, HA, and OD-3 drilling cores (partially modified from Uchiyama et al. (2001)).

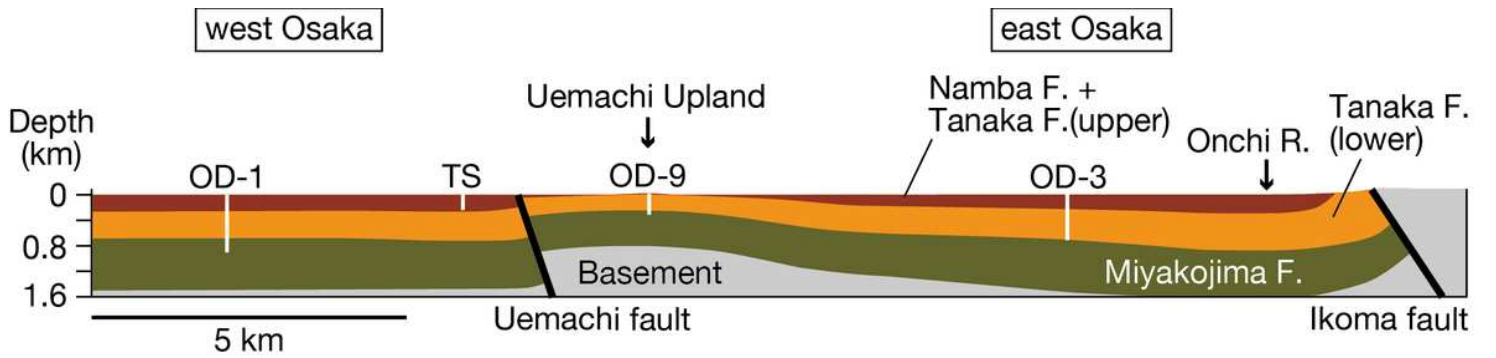


Figure 3

Figure 3

Schematic E-W geological section through the Osaka Plain (Uchiyama et al. 2001).

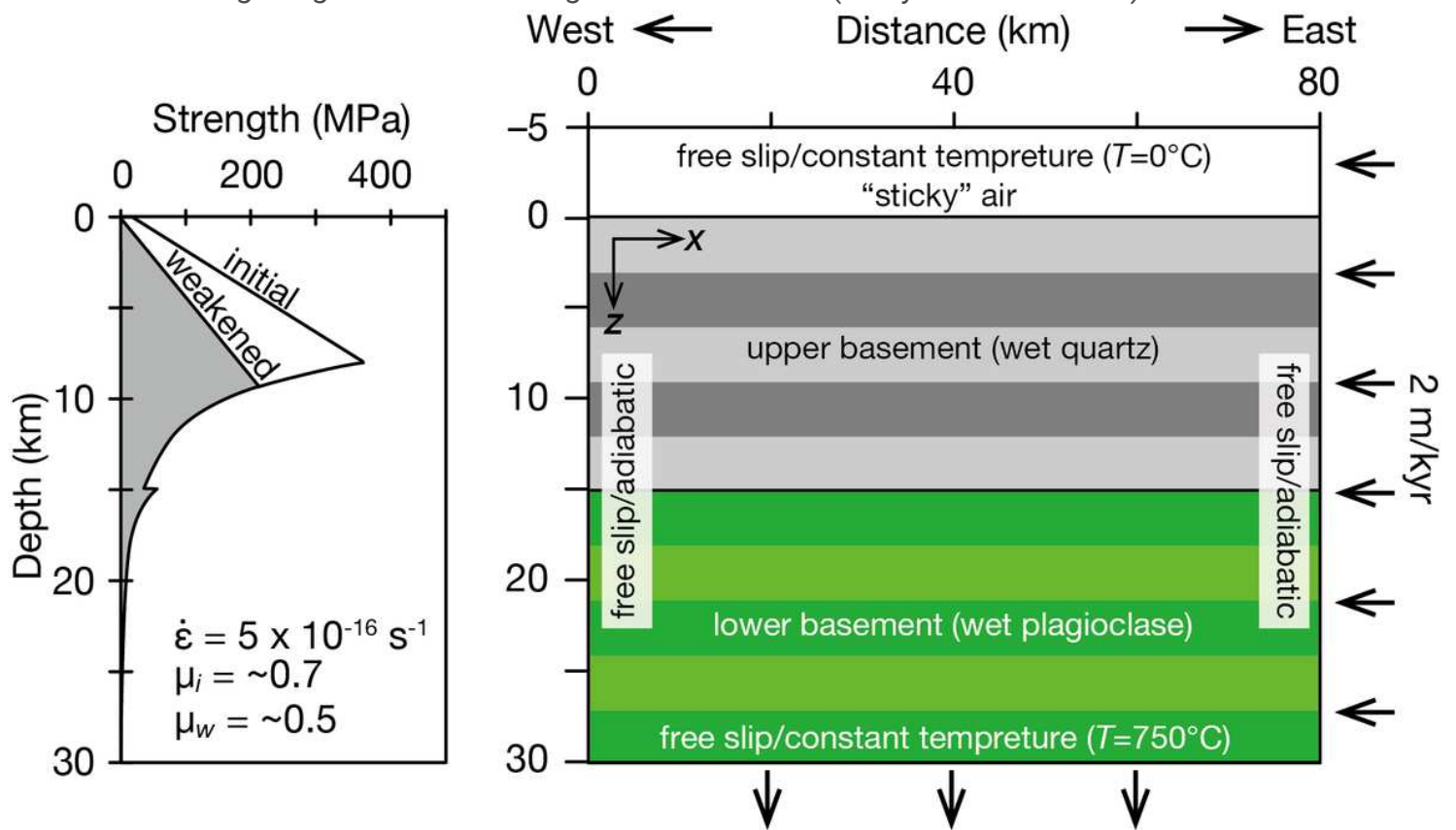


Figure 4

Figure 4

Model geometry and boundary conditions. The inset shows the crustal strength profile at the initial state in the numerical model.  $\dot{\epsilon}$ ,  $\mu_i$ , and  $\mu_w$  are the strain rate, the initial friction coefficient, and the weakened friction coefficient, respectively. A changing downward velocity (from 0.88 m/kyr at 0 Myr to 1.02 m/kyr at 3 Myr) is applied at the bottom boundary.

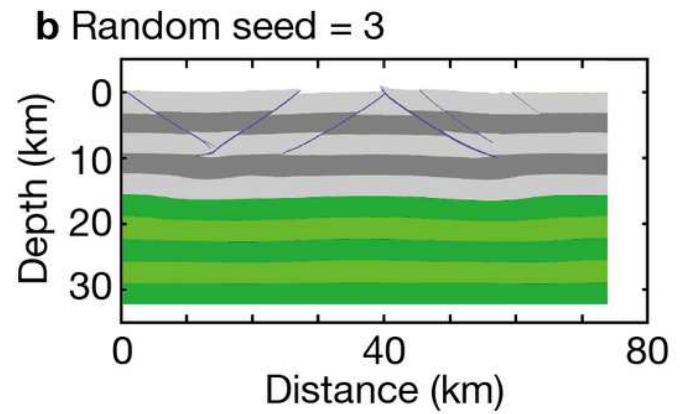
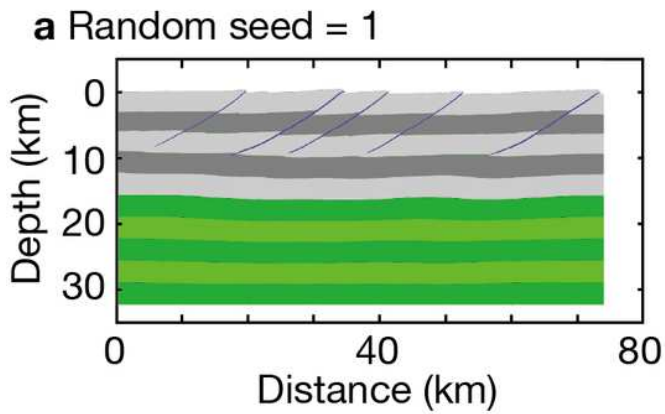


Figure 5

Figure 5

Results at 3 Myr for the numerical simulations with no preexisting fault zone. The newly formed faults (markers with a cumulative strain larger than 1) are illustrated in dark blue. a Case with the random seed number = 1. b Case with the random seed number = 3.

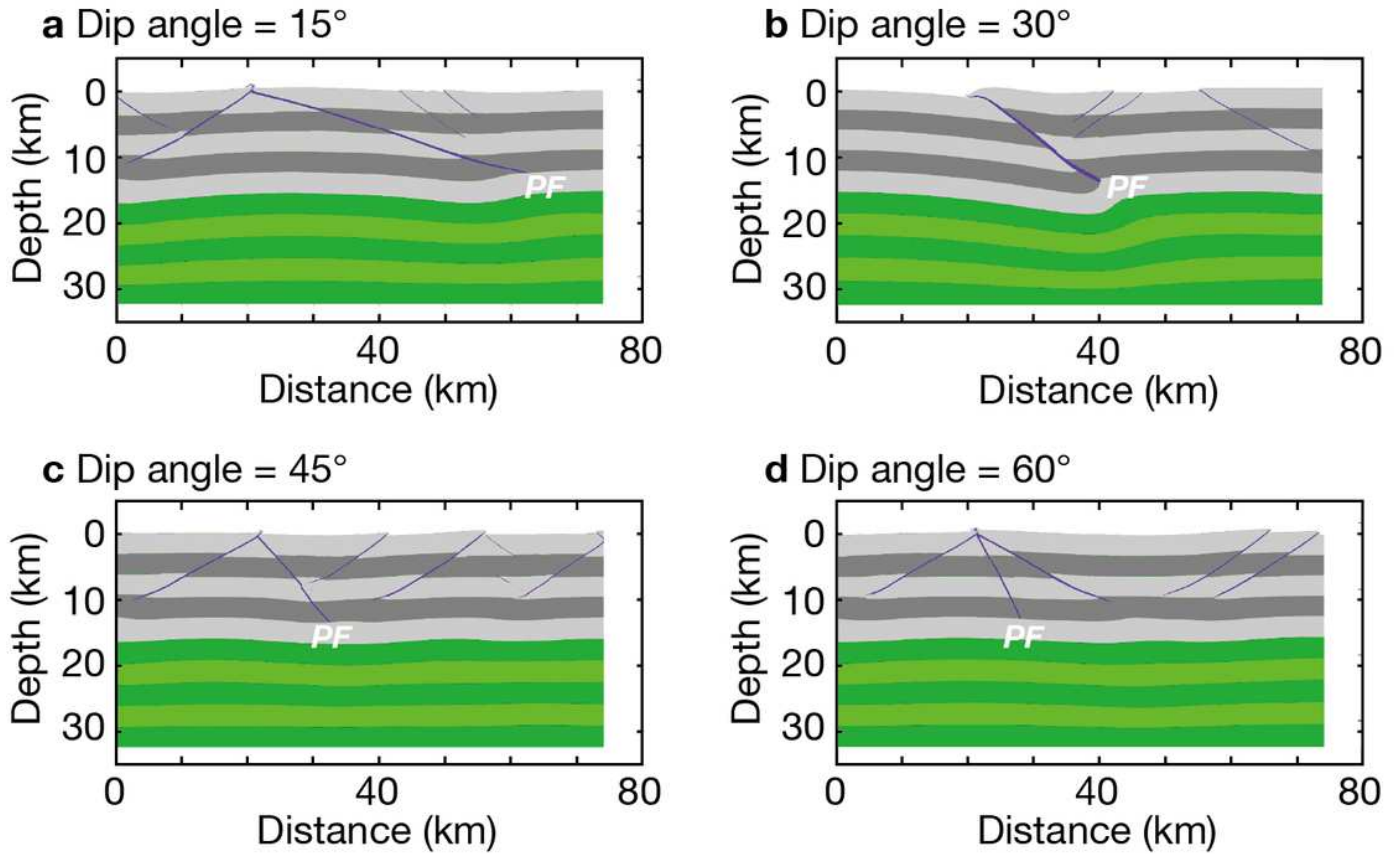


Figure 6

Figure 6

Results at 3 Myr for numerical simulations with a single preexisting fault zone. The preexisting fault (PF) and the newly formed faults (markers with a cumulative strain larger than 1) are illustrated in dark blue. The weakened friction coefficient  $\mu_w$  is  $\sim 0.5$  (weakened friction angle  $\phi_w = 30^\circ$ ). a Case with a dip angle of  $15^\circ$ . b Case with a dip angle of  $30^\circ$ . c Case with a dip angle of  $45^\circ$ . d Case with a dip angle of  $60^\circ$ .

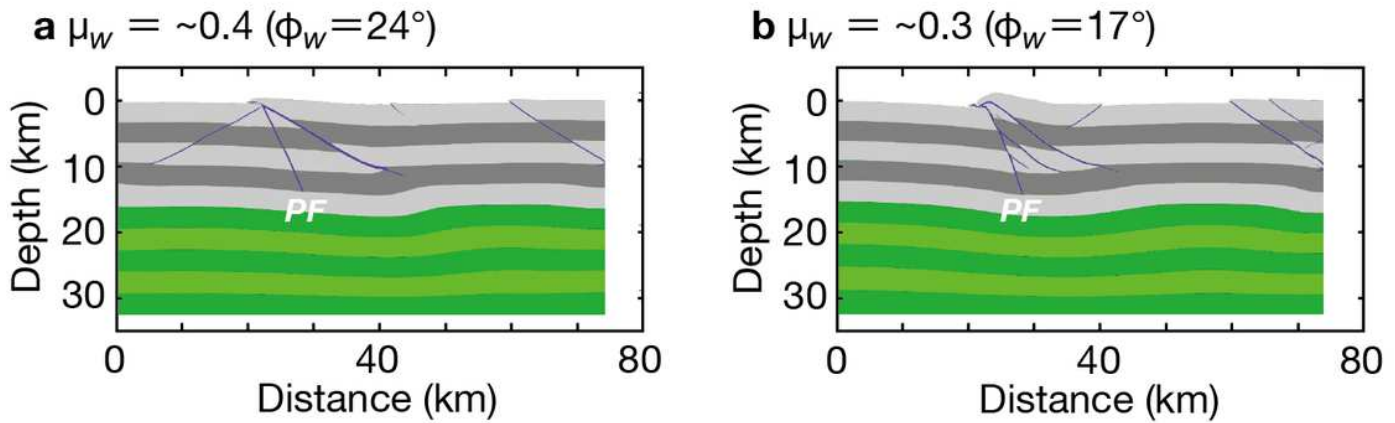


Figure 7

Figure 7

Effect of different weakened friction coefficients  $\mu_w$  on the activity of a preexisting fault with a dip angle of  $60^\circ$ . a Case with  $\mu_w = \sim 0.4$  (weakened friction angle  $\phi_w = 24^\circ$ ). b Case with  $\mu_w = \sim 0.3$  ( $\phi_w = 17^\circ$ ). The preexisting fault (PF) and newly formed faults (markers with a cumulative strain larger than 1) are illustrated in dark blue.

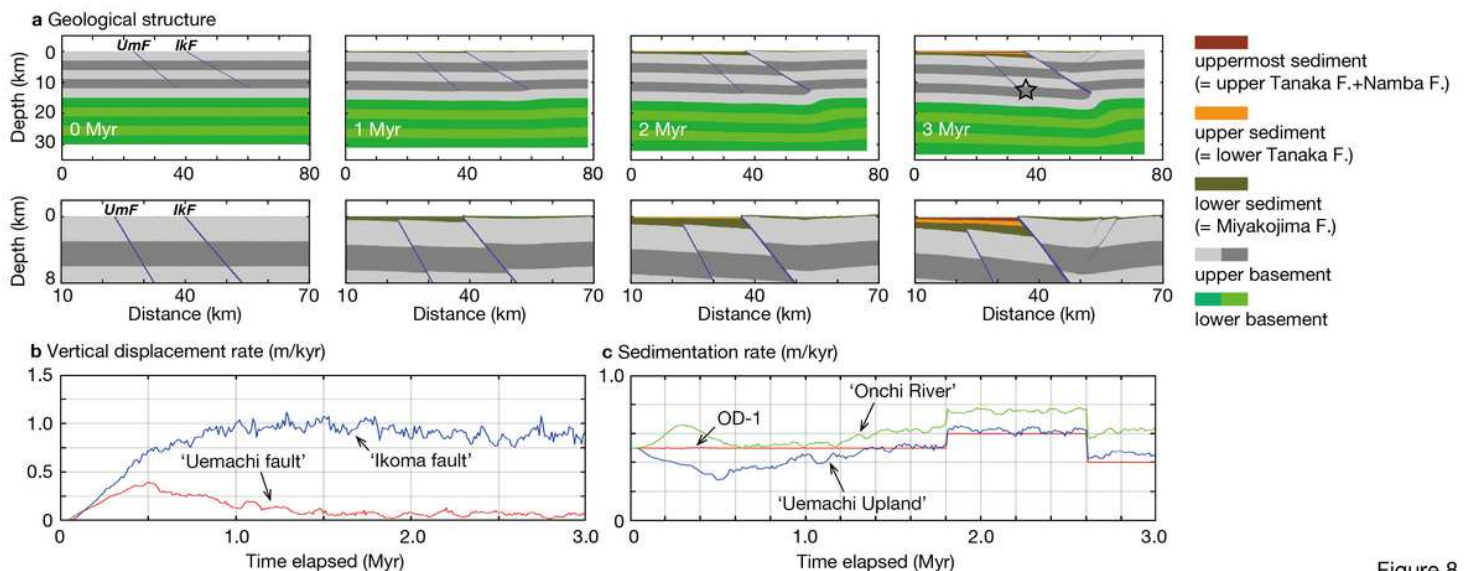


Figure 8

Figure 8

Results of the numerical simulation for a case with two preexisting fault zones with dip angles of  $40^\circ$  and  $30^\circ$ , corresponding to the Uemachi and Ikoma faults in the Osaka Plain, respectively. a The initial model geometry and time evolution. The epicenter of the 2018 northern Osaka earthquake (Kato and Ueda

2019), located 12 km beneath the surface position 14 km from the Uemachi fault, is indicated by a star. The lower panels show a close up view of a 60 km × 10 km domain including the western and eastern weak zones. The preexisting faults and newly formed faults (markers with a cumulative strain larger than 1) are illustrated in dark blue. b Time evolution of the vertical displacement rates along the western and eastern faults. c Time evolution of the sedimentation rates near the Uemachi Upland (i.e., at the location of the OD-9 core site) and the Onchi River (i.e., at the location of the OD-3 core site). The imposed sedimentation rates at the location of the OD-1 core site are also shown.

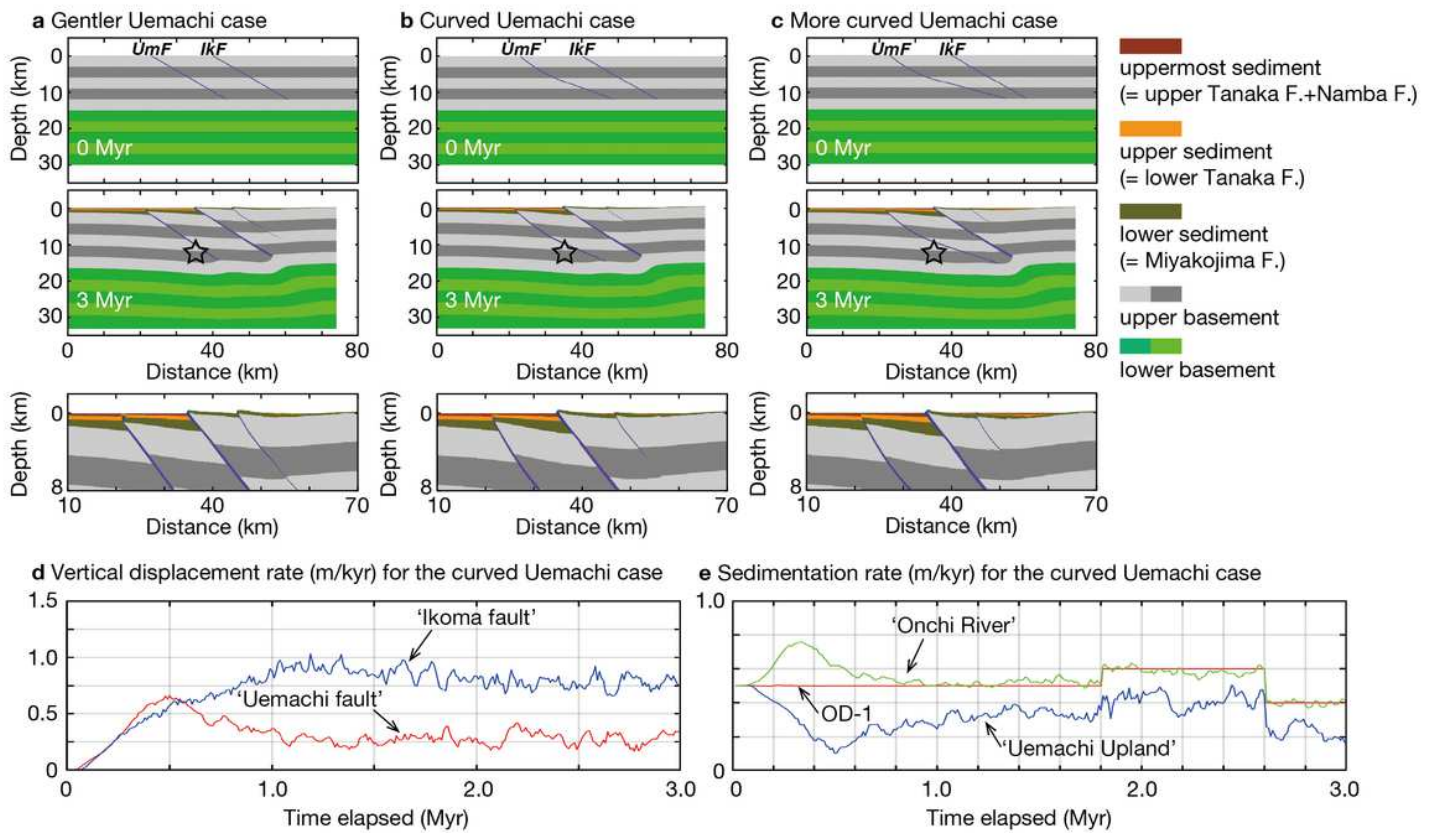


Figure 9

Figure 9

Effect of changing the dip angle of the western fault (i.e., the Uemachi fault) on the development of the geologic structures. a The initial geometry (upper), final geometry (middle), and close up of the final geometry (lower) of the linear case with a dip angle of 30°. b The initial geometry (upper), final geometry (middle), and close up of the final geometry (lower) of the curved case. c The initial geometry (upper), final geometry (middle), and close up of the final geometry (lower) of the more curved case. The preexisting faults and newly formed faults (markers with a cumulative strain larger than 1) are illustrated in dark blue. The epicenter of the 2018 northern Osaka earthquake (Kato and Ueda 2019), located 12 km beneath the surface position 14 km from the Uemachi fault, is indicated by a star in the panels showing the result at 3 Myr. d Time evolution of the vertical displacement rates along the western and eastern faults for the curved case. e Time evolution of the sedimentation rates near the Uemachi Upland (i.e., at

the location of the OD-9 core site) and the Onchi River (i.e., at the location of the OD-3 core site) for the curved case. The imposed sedimentation rates at the location of the OD-1 core site are also shown.

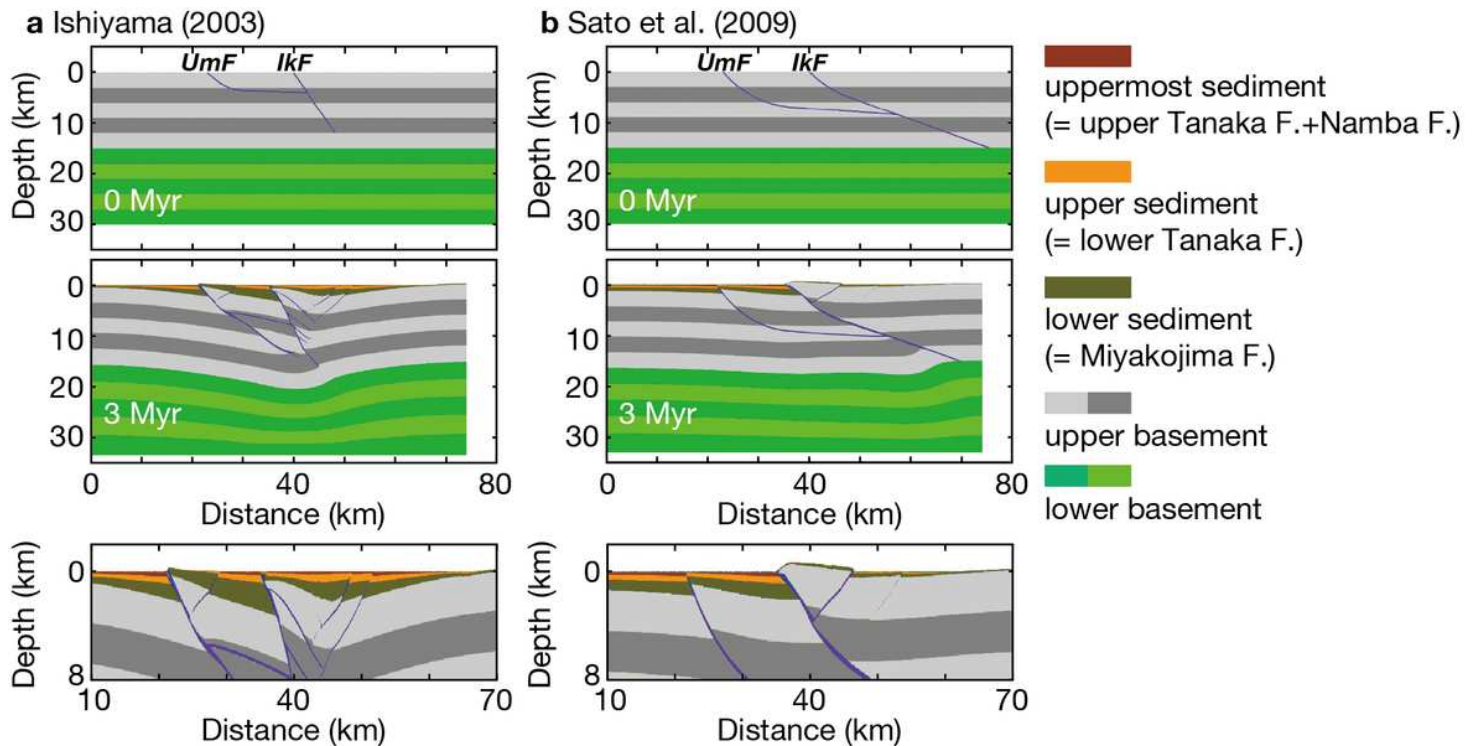


Figure 10

Figure 10

Results of the numerical simulations for previously proposed fault geometries. a The initial geometry (upper), final geometry (middle), and close up of the final geometry (lower) for the fault geometry of Ishiyama (2003) with a weakened friction coefficient  $\mu_w$  of  $\sim 0.3$  (weakened friction angle  $\varphi_w = 17^\circ$ ). b The initial geometry (upper), final geometry (middle), and close up of the final geometry (lower) for the fault geometry of Sato et al. (2009) with  $\mu_w = \sim 0.4$  ( $\varphi_w = 24^\circ$ ). The preexisting faults and newly formed faults (markers with a cumulative strain larger than 1) are illustrated in dark blue. UmF and IkF represent the surface positions of the Uemachi and Ikoma faults, respectively.

## Supplementary Files

This is a list of supplementary files associated with this preprint. Click to download.

- [Table1.docx](#)
- [GraphicalAbstract.png](#)
- [Additionalfile1.docx](#)